The Forward Time-of-Flight System for CLAS12

D.S. Carman [a,1], R. Gothe [b], L. Clark [c] R. De Vita [d] B. Miller [a], and C. Wiggins [a]

[a] *Thomas Jefferson National Accelerator Facility, Newport News, VA 23606, USA*

[b] *University of South Carolina, Columbia, SC 29208, USA*

[c] *University of Glasgow, Glasgow G12 8QQ, United Kingdom*

[d] *INFN, Sezione di Genova, 16146 Genova, Italy*

Abstract

The Forward Time-of-Flight system for the large-acceptance CLAS12 spectrometer in Hall B at the Thomas Jefferson National Accelerator Facility is described. The system is positioned ∼6-7 m from the beam-target interaction point and spans laboratory polar angles from $\sim 5^\circ \rightarrow 35^\circ$ and nearly the full azimuth. The system consists of 540 individual scintillation counters with double-ended readout that range in length from 17 cm to 426 cm of discrete widths of 6 cm, 15 cm, and 22 cm, and of discrete thicknesses of 5 cm and 6 cm. The effective counter time resolution for passing charged particles varies from ∼50 ps for the shortest counters at small angles to ∼150 ps for the longest counters at large angles. The detectors are part of the overall CLAS12 Forward Detector particle identification scheme during offline event reconstruction and are part of the online data acquisition trigger to select final state event topologies with charged hadrons.

PACS:29.40.Mc

Keywords: CLAS12, time of flight, plastic scintillator, particle identification

[1] Corresponding author. Address: 12000 Jefferson Ave., Newport News, VA; e-mail: carman@jlab.org.

Contents

1 Overview of CLAS12

The Thomas Jefferson National Accelerator Facility (JLab) recently completed a project to double the maximum energy of its electron accelerator from 6 GeV to 12 GeV. The experimental equipment in Hall B forms the large-acceptance CLAS12 spectrometer that is designed to operate with beam energies up to 11 GeV at a nominal beam-target luminosity of 1×10^{35} cm^{-2}s^{-1} to allow for precision measurements of exclusive reactions with polarized beam and both unpolarized and polarized targets. This spectrometer is based on two superconducting magnets, a solenoid in the central region about the target and a toroid at forward angles.

The CLAS12 torus has a six-fold symmetry that divides the forward acceptance in the polar angle range from 5° to 35° into six 60°-wide sectors. It produces a field primarily in the azimuthal direction. The torus $\int Bd\ell$ field strength at its nominal full current is 2.8 T at 5° and 0.5 T at 35°. A set of three multi-layer drift chambers in each sector (before the field, within the field, and after the field) and a forward micromegas vertex tracker are used for charged particle tracking to measure momenta. Downstream of the torus each sector is instrumented with a Cherenkov counter for π/K separation (five sectors are instrumented with low threshold gas Cherenkov counters and one sector is instrumented with a ring-imaging Cherenkov counter), three planar layers of scintillation counters for charged particle timing measurements called the Forward Time-of-Flight (FTOF) system, and an electromagnetic calorimeter system for electron and neutral particle identification. Just upstream of the torus is a large-volume high-threshold gas Cherenkov counter for electron identification and a tagging system to detect electrons and photons at scattering angles below 5°.

The CLAS12 solenoid spans the central angular range from 35° to 125° and has a uniform 5 T central field. The solenoid serves to focus the low-energy Møller background down the beam pipe to the beam dump away from the acceptance of the spectrometer. The detectors mounted within the solenoid include a thick scintillation counter for neutron identification, a barrel of thin scintillation counters for charged particle timing measurements, and a set of tracking detectors about the target. Upstream of the solenoid, covering angles from 135° to 145° a wall of scintillation counters is installed for additional neutron detection coverage.

Fig. 1 shows a model representation of CLAS12 to highlight its overall layout and scale. The CLAS12 spectrometer was installed and instrumented in Hall B in the period from 2012 to 2018. The CLAS12 spectrometer took the place of the original CLAS spectrometer [1] that operated in Hall B in the period from 1997 to 2012 when it was decommissioned.

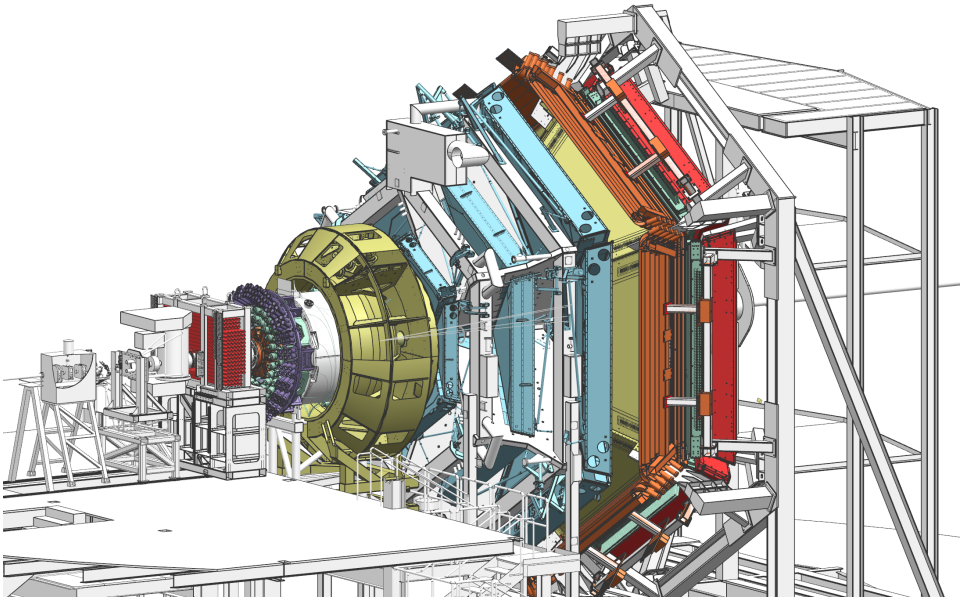

Fig. 1. (Color Online) Model representation of the CLAS12 spectrometer in Hall B at Jefferson Laboratory. The electron beam is incident from the left side of this figure. The CLAS12 detector is roughly 10 m in scale along the beam axis. For further details on the individual subsystems that make up the CLAS12 spectrometer see Ref. [2].

This paper focuses on the CLAS12 FTOF detector system and is organized as follows: Section 2 reviews the scheme for particle identification in the CLAS12 Forward Detector, Section 3 provides a high-level overview of the FTOF system and its overall design requirements, Section 4 provides a technical description of the system design, and Section 5 highlights the performance of the system through both bench testing with cosmic rays, as well as during the 2017 commissioning run and 2018 first production run with electrons. Finally, Section 6 provides a summary of the FTOF system for CLAS12.

2 CLAS12 Forward Detector Particle Identification

Particle identification in the CLAS12 Forward Detector relies on input from each of the different forward detector subsystems. A reconstructed track in the Drift Chambers (DC) identifies the presence of a charged particle and is used as a veto for forward-going neutral particles. The curvature of the particle tracks in the magnetic field of the torus provides the electric charge. The other detector subsystems are used to identify the particle type. These subsystems include the different Cherenkov counters (HTCC, LTCC, and RICH), the electromagnetic calorimeters (ECAL), and the FTOF system. These systems are used as part of the overall CLAS12 particle identification scheme to separate the different particle species as a function of momentum.

CLAS12 consists of three different Cherenkov counters in the Forward Detector. A CO_2 filled High Threshold Cherenkov Counter (HTCC) is positioned just downstream of the solenoid magnet. The HTCC is used in conjunction with the electromagnetic calorimeters (ECAL) to identify scattered electrons over their full momentum range. The HTCC threshold for pions is $\sim$5 GeV and is therefore used for e/π discrimination up to this threshold. The HTCC is also used for π/K and π/p separation from $\sim$5-9 GeV. The C_4F_{10} filled Low Threshold Cherenkov Counter (LTCC) is included in four of the six CLAS12 sectors just upstream of the FTOF. This system is used for π/K and π/p separation for particle momenta in the range from $\sim$3-9 GeV. Finally, an aerogel-based Ring Imaging Cherenkov (RICH) detector is included in one sector of CLAS12 and is used for π/K, π/p, and K/p separation in the range of momenta from $\sim$3-8 GeV.

However, the primary system for particle identification in CLAS12 for forward-going charged particles is the FTOF system. The main requirement for this system is that its counters provide excellent timing resolution for particle identification. The FTOF was designed to measure the flight time of charged particles emerging from the target with an average timing resolution of 80 ps. Given this nominal timing resolution for the counters, the momentum threshold for particle identification can be defined. For our purposes, thresholds are quoted at the 4σ level for FTOF, which amounts to the momenta where particle identification can occur with up to an order of magnitude difference in the relative yields of the different species. The timing resolution is illustrated by computing the flight time differences between different charged particle species, pions, kaons, and protons, for tracks normally incident on the detector. Fig. 2 shows the computed time differences as a function of momentum. Where the 4σ line crosses the computed time difference curves defines the momentum limit for particle identification for each particle species. These limits are quoted as 2.8 GeV for π/K separation, 4.8 GeV for K/p separation, and 5.4 GeV for π/p separation. Fig. 3 shows the different detector subsystems used for charged particle identification of forward-going charged particles in CLAS12 and the range of momenta for which they are responsible for the separation of the different particle species.

Fig. 4 shows a plot of the momentum versus polar angle in CLAS12 from beam data of an 11 GeV electron beam incident on a hydrogen target for a typical exclusive reaction $ep \rightarrow e'K^+\Lambda$. For this reaction the typical charged hadron track momenta accepted by FTOF are in the range from 1 GeV to 7 GeV.

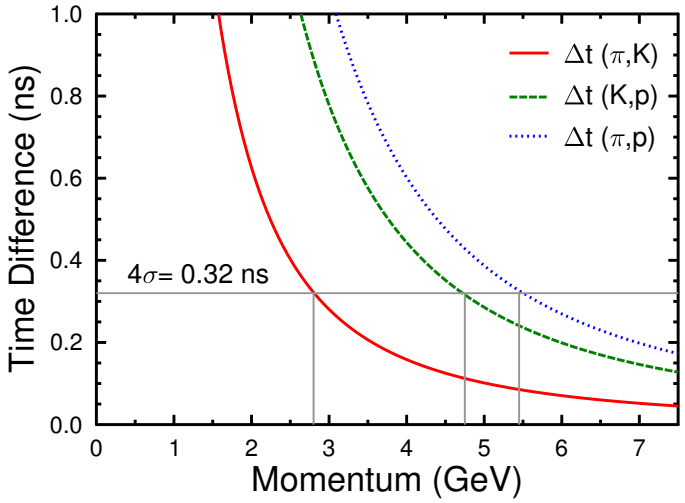

Fig. 2. (Color Online) Time differences, Δt, between protons and pions, between protons and kaons, and between kaons and pions (as indicated) over the ∼6-7 m path length from the target to the FTOF system. The horizontal line indicates a time difference four times larger than the average FTOF counter design resolution of $\sigma_{TOF} \approx 80$ ps. The vertical line that meets each curve represent the momentum where 4σ particle species separation is quoted.

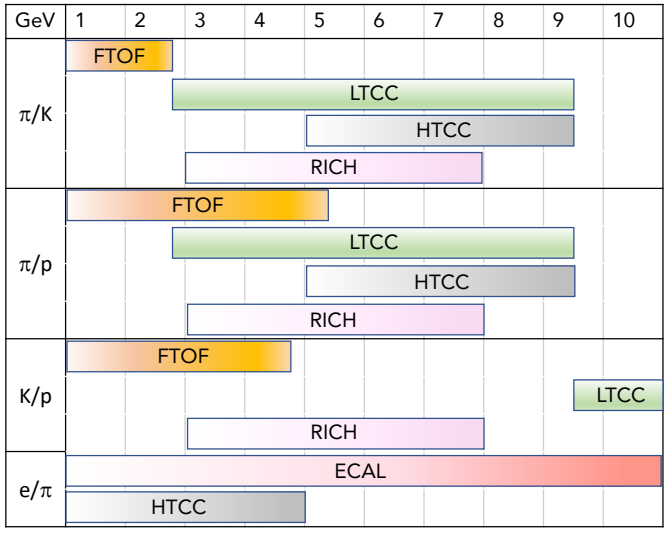

Fig. 3. (Color Online) CLAS12 Forward Detector subsystems used for particle identification and the range of momentum where they are effective in separating different particle species.

3 Overview of the FTOF System

The Forward Time-of-Flight System (FTOF) is a major component of the CLAS12 Forward Detector used to measure the time-of-flight of charged par-

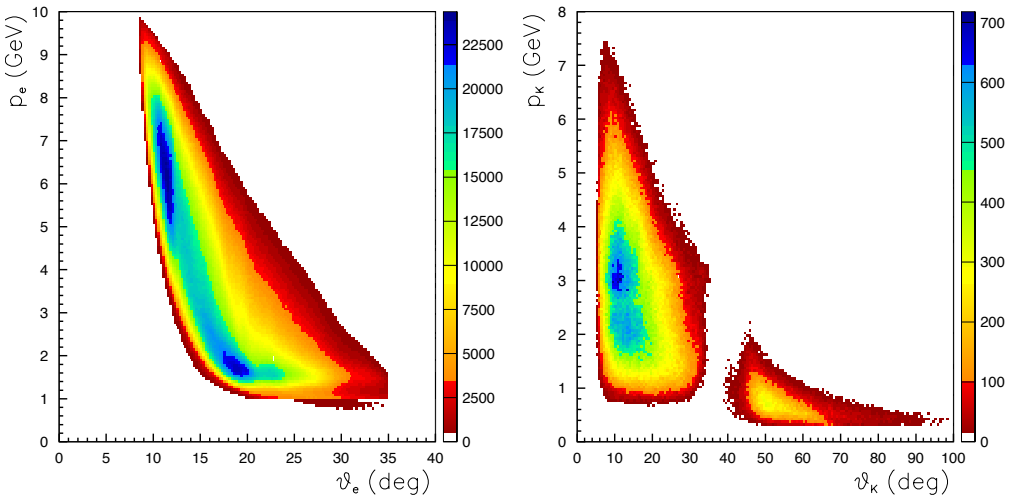

Fig. 4. (Color Online) Plot of momentum vs. angle from beam data for a 10.6 GeV electron beam incident upon a liquid-hydrogen target in CLAS12 for selection of a final-state electron (left) and K^+ (right). The discontinuity at $\theta = 35°$ is due to the small acceptance gap between the Forward and Central Detectors. The typical momentum of charged tracks in the Central Detector is less than 2 GeV.

ticles emerging from interactions in the target. The requirements for FTOF include excellent timing resolution for charged particle identification and good segmentation to minimize counting rates and to provide for flexible triggering options. The system specifications call for an average time resolution of σ_{TOF}=80 ps at the more forward angles of CLAS12 and 150 ps at angles larger than 35°. The system must also be capable of operating in a high-rate environment where the average counting rate for each FTOF scintillator at an operating luminosity of 1×10^{35} cm^{-2}s^{-1} is ∼0.5-1 MHz.

In each of the six sectors of the CLAS12 Forward Detector, the FTOF system is comprised of three arrays of counters, referred to as panels, named panel-1a, panel-1b, and panel-2. Each panel consists of a set of rectangular scintillators with a photomultiplier tube (PMT) on each end. Panel-1 refers to the counters located at forward angles (roughly 5° to 35°) (where two panels are employed to meet the 80 ps average time resolution requirement) and panel-2 refers to the sets of counters at larger angles (roughly 35° to 45°). The positioning and attachment of the FTOF detector arrays on their Forward Carriage supports are shown in Fig. 5.

The FTOF counters in the angular range from 5° to 35° consist of two sets of six triangular arrays. Just upstream of the electromagnetic calorimeter (ECAL) detectors, the panel-1a arrays are mounted. These detector sets were refurbished from the panel-1 TOF counters from the decommissioned CLAS spectrometer [3]. Upstream of the panel-1a arrays the new panel-1b arrays are mounted. In the event reconstruction the hit times for panel-1a and panel-1b are combined together to determine the charged particle hit time (see

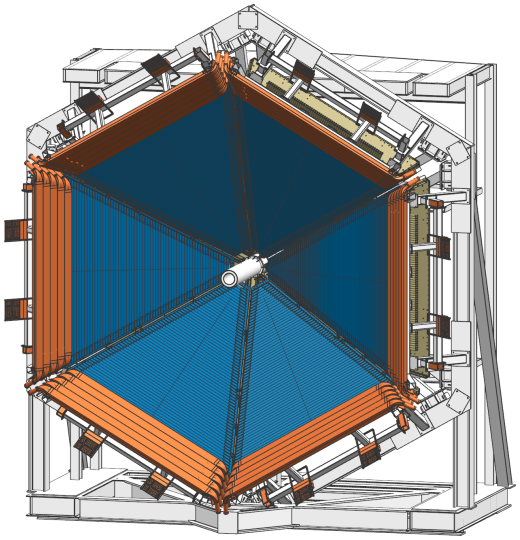

Fig. 5. (Color Online) View of the FTOF counters for CLAS12 highlighting the location of the panel-1 and panel-2 counters. The panel-1b counter arrays are shown in blue and the panel-2 counter arrays, mounted around the perimeter of the Forward Carriage, are shown in orange. The panel-1a counter arrays mounted just downstream of the panel-1b arrays are not visible in this picture. The Forward Carriage is roughly 10 m in diameter.

Section 5.2.8). In the angular range from 35° to 45° the panel-2 arrays are mounted. These counters were refurbished from the panel-2 arrays of the CLAS TOF system. A detailed summary of the FTOF technical parameters is given in Table 1.

The panel-1 arrays consist of the old CLAS panel-1 TOF counters (called panel-1a) and a new set of panel-1 counters (called panel-1b). The panel-1a arrays consist of 23 scintillators, each measuring 5.08-cm thick and 15-cm wide. The lengths of these counters range from roughly 32 cm at the smallest scattering angles to roughly 376 cm at the largest scattering angles. The scintillators are constructed from Bicron [4] BC-408 and are read out through short acrylic light guides to 2-in Thorn EMI-9954A PMTs. The new panel-1b arrays consist of 62 scintillators constructed from Bicron BC-404 scintillator for the shorter counters and BC-408 for the longer counters, each 6-cm wide and 6-cm thick. The lengths of these counters range from roughly 17 cm at the smallest scattering angles to roughly 408 cm at the largest scattering angles. The scintillators are read out through Hamamatsu R9779 PMTs [5] coupled directly to the scintillation bars. This new panel is mounted to the Forward Carriage in front of the panel-1a counters. The detailed design and bench testing results for these counters is described in detail in Ref. [6].

The panel-2 arrays consist of selected counters from the old CLAS panel-2 TOF counters, and include 5 22-cm wide, 5.08-cm thick scintillators in each sector. The length of these counters ranges from roughly 370 cm to 440 cm. These scintillators are constructed from Bicron BC-408 and are read out

Parameter	Design Value
Panel-1a	
Angular Coverage	$\theta = 5^\circ \rightarrow 35^\circ$, ϕ : 50% at $5^\circ \rightarrow$ 85% at 35°
Counter Dimensions	$L = 32.3$ cm $\rightarrow 376.1$ cm, $w \times h = 15$ cm $\times$ 5 cm
Scintillator Material	BC-408
PMTs	EMI 9954A, Philips XP2262
Design Resolution	90 ps $\rightarrow$ 160 ps
Panel-1b	
Angular Coverage	$\theta = 5^\circ \rightarrow 35^\circ$, ϕ : 50% at $5^\circ \rightarrow$ 85% at 35°
Counter Dimensions	$L = 17.3$ cm $\rightarrow 407.9$ cm, $w \times h = 6$ cm $\times$ 6 cm
Scintillator Material	BC-404 (#1 $\rightarrow$ #31), BC-408 (#32 $\rightarrow$ #62)
PMTs	Hamamatsu R9779
Design Resolution	60 ps $\rightarrow$ 110 ps
Panel-2	
Angular Coverage	$\theta = 35^\circ \rightarrow 45^\circ$, ϕ : 85% at $35^\circ \rightarrow$ 95% at 45°
Counter Dimensions	$L = 371.3$ cm $\rightarrow 426.1$ cm, $w \times h = 22$ cm $\times$ 5 cm
Scintillator Material	BC-408
PMTs	Photonis XP4312B, EMI 4312KB
Design Resolution	145 ps $\rightarrow$ 160 ps

Table 1
Table of parameters for the scintillators, PMTs, and counters for the FTOF panel-1a, panel-1b, and panel-2 arrays.

through curved acrylic light guides to 3-in Philips XP4312B PMTs. These scintillators are included to give complete acceptance for outbending charged particles incident upon the CLAS12 drift chambers.

4 FTOF System Design

In order to meet the performance and mechanical requirements for the FTOF system, the major considerations in its design included the system geometry and areal coverage, the counter and system timing resolutions, the system components, and the design and materials associated with its mechanical support structure in the active area of the spectrometer. These system design elements are described in the following subsections. In addition, this section

also includes information on the readout electronics and the high voltage system used for the FTOF.

4.1 Geometry

The projected space behind the coils of the CLAS12 torus as defined by straight lines projecting from the center of the nominal target position radially outward and is referred to downstream of the torus as its shadow region. This region is inactive and defines the space available for locating the light guides, photomultiplier tubes (PMTs), voltage dividers, and signal and high voltage cables. The remaining area in the forward direction is the sensitive fiducial region of the detector and must be covered with scintillation counters. The design specification for FTOF called for a minimum of 50% azimuthal acceptance at 5° increasing to 95% at 45°.

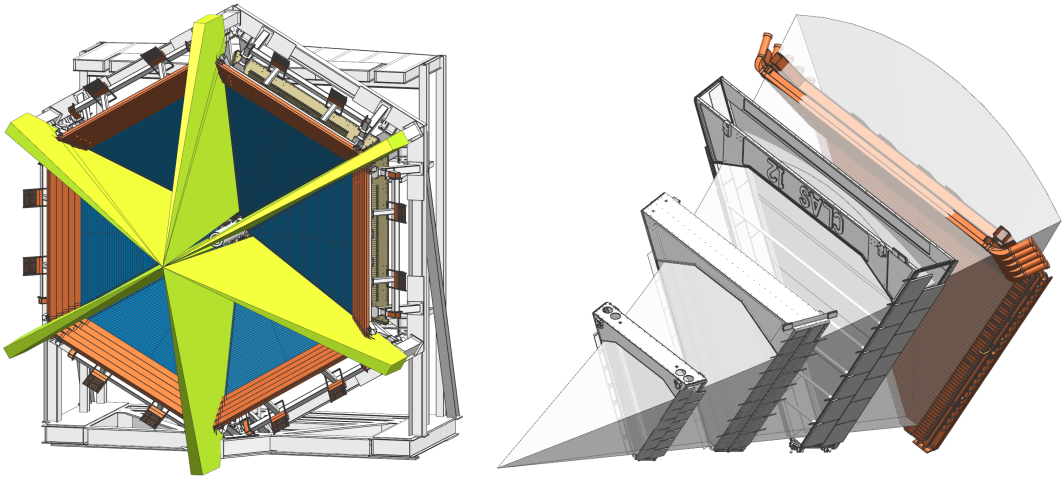

Fig. 6. (Color Online) (Left) View of the shadows created by the main torus cryostats and drift chamber endplates as projected on the face of the FTOF system. (Right) The defined active area between the shadow projections through the three regions of drift chambers projected on the face of the FTOF in a representative Forward Carriage sector.

Fig. 6 provides an illustration of the shadow region projected onto the Forward Carriage created primarily by the torus cryostats and the drift chamber endplates as projected on the face of the FTOF system. These pictures come from the CAD design model of CLAS12. Fig. 6(left) shows a picture of the shadow bands on the Forward Carriage that defines a uniform gap of ∼40 cm between each sector. Fig. 6(right) shows the defined active region in one sector of CLAS12 on the face of the FTOF. The width of this area in azimuth at the position of the Forward Carriage in Hall B essentially defined the length of the scintillation counters. The final limits of the shadow region at the location of FTOF are actually defined by the Region 2 Drift Chamber system. While the

Region 1 and Region 3 chambers have their endplates, on-board electronics, and readout cables located mainly in the shadow of the torus cryostats, the Region 2 chambers are located fully between the cryostats.

The panel-1a and panel-1b FTOF arrays in each sector are triangular in shape with the shortest counters located closest to the beamline and the longest counters furthest from the beamline. The length of each counter for a given counter number $N_{counter}$ is as follows:

- Panel-1a: $L(cm) = 15.85 \times N_{counter} + 16.43 \quad (N_{counter} = 1 \rightarrow 5)$,
- Panel-1a: $L(cm) = 15.85 \times N_{counter} + 11.45 \quad (N_{counter} = 6 \rightarrow 23)$,
- Panel-1b: $L(cm) = 6.40 \times N_{counter} + 10.84 \quad (N_{counter} = 1 \rightarrow 62)$.

The panel-1a and panel-1b arrays are tilted toward the target at an angle of 25° consistent with the other subsystems in the CLAS12 Forward Detector (DC, LTCC, RICH, ECAL). The panel-1a counters are located at a radial distance of the target in the range from R=724.21 cm for $N_{counter} = 1$ to R=691.74 cm for $N_{counter} = 23$. The panel-1b counters are located at a radial distance from the target in the range from R=716.15 cm for $N_{counter} = 1$ to R=677.97 cm for $N_{counter} = 62$. The gap between the coplanar panel-1b and panel-1a arrays in each sector is 10.72 cm. The minimum angle covered by panel-1a based on a straight line from the target is 5.453°. The corresponding minimum angle covered by panel-1b is 3.667°. Each of the panel-1a arrays covers an area of 7.0 m^2 and each of the panel-1b arrays covers an area of 7.9 m^2. Fig. 7 shows a two-dimensional schematic of the layout and positioning of the arrays defining the key geometry parameters, which are listed in Table 2. See Ref. [7] for more information.

The panel-2 arrays are mounted radially outward of the panel-1a and panel-1b arrays as shown in Fig. 7. The length of each counter for a given counter number $N_{counter}$ is as follows:

- Panel-2: $L(cm) = 13.73 \times N_{counter} + 357.55 \qquad (N_{counter} = 1 \rightarrow 5)$.

The panel-2 arrays are tilted toward the target at an angle of 58.11°. The minimum angle covered by panel-2 based on a straight line from the target is 34.698°. Each of the six panel-2 arrays covers an area of 4.4 m^2. Note that the panel-2 arrays are not visible in the CLAS12 acceptance as seen by straight lines from the center of the target. However, due to the presence of the toroidal magnetic field, they provide additional acceptance for low momentum tracks and for tracks associated with strange particles that decay in-flight after emerging from the target (e.g. $\Lambda \rightarrow N\pi$ with $c\tau = 7.89$ cm).

Given the active area coverage requirements for the FTOF system within each CLAS12 sector on the Forward Carriage, another key aspect of the geometry associated with the FTOF system design is the width of the individual scin-

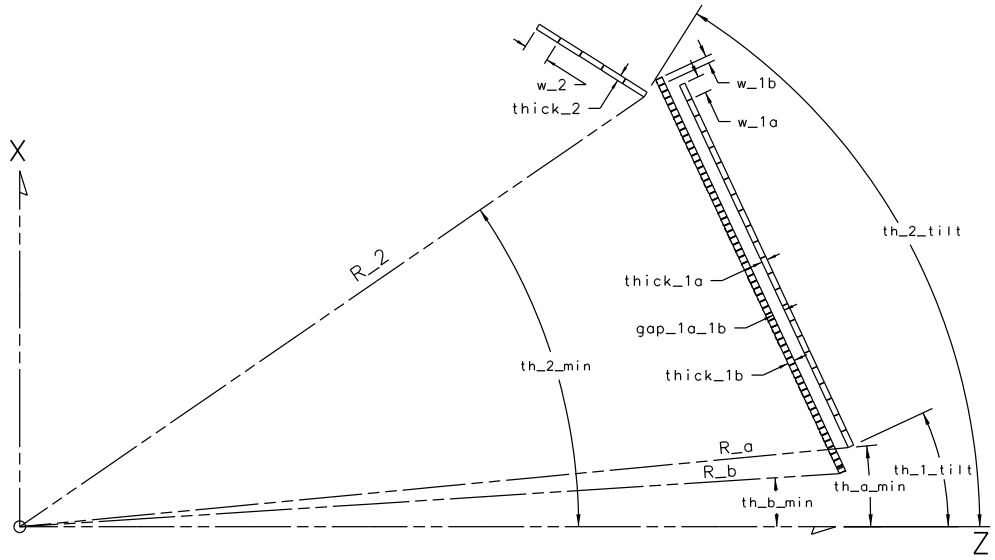

Fig. 7. View of the FTOF scintillators for panel-1a, panel-1b, and panel-2 in the sector mid-plane for one representative sector of the CLAS12 Forward Detector with the key parameters indicated.

Parameter	Nominal Value		
R	726.689 cm	717.236 cm	659.71 cm
th_min	5.453°	3.667°	34.698°
th_tilt	25.00°	25.00°	58.11°
thick	5.08 cm	6.00 cm	5.08 cm
width	15.00 cm	6.00 cm	22.00 cm
gap_1a_1b	10.717 cm		–

Table 2
Table of the nominal geometry parameters for the CLAS12 FTOF detector system.

tillation counters. An essential optimization was made to select the counter width to reduce the number of readout channels while considering the overall counting rates per bar at the nominal luminosity associated with incident charged and neutral particles including photons. These rates must allow for reasonable PMT anode currents that do not affect the stability of the PMT response in terms of pulse shape or saturation effects, or lead to unreasonably short PMT lifetimes defined in terms of the total integrated charge collected at the first dynode of the PMT. In addition, the width of the scintillation bars determines the granularity of the scattering angle definition in the trigger and its matching to the projected tracks from the Drift Chambers and toward the electromagnetic calorimeters. Note that the 15 cm widths of panel-1a and the 22 cm widths of panel-2 from the existing refurbished counters from the CLAS TOF system were optimized for nominal beam-target luminosities a factor of 10 lower than for CLAS12. The 6 cm widths of the newly constructed panel-1b

counters were optimized for the higher rate operating conditions of CLAS12.

4.2 Time Resolution

Time-of-flight detectors are designed to provide an output signal for the data acquisition system that reflects the time a charged particle passed through the scintillation counter. As the particle passes through the scintillation material, it causes ionization that subsequently generates scintillation light. The photons that are created travel on various paths inside of the scintillator and light guide (if present), which may get absorbed, reflected (internally or on outer wrapping materials), and ultimately impinge on the photocathode of the PMT. This interaction produces a photoelectron signal that is amplified within the stages of the PMT and this pulse is then input into the readout electronics, which includes a discriminator and a time-to-digital (TDC) converter. The net effect of these different processes accounts for the time resolution of the counter σ_{TOF}.

The contributions to the time resolution of TOF systems have been parameterized in Ref. [8] using the following form:

$$\sigma_{TOF} = \sqrt{\sigma_0^2 + \frac{\sigma_1^2 + (\sigma_2 L/2)^2}{N_{pe}}}. \quad (1)$$

Here σ_0 represents the intrinsic electronic resolution of the measurement system. This represents a floor-term contribution that is independent of light level. The remaining terms σ_1 and σ_2 are directly dependent on the photostatistics at the PMT photocathode N_{pe}. The term σ_1 models the jitter in the combined single photoelectron response of the scintillation counter and its PMTs and the term σ_2 accounts for path length variations in the light collection. These path length variations in the scintillator scale with the distance from the source to the PMT, which we take to be half the length of the counter $(L/2)$, since the scintillators are read out at either side. The statistical behavior of the last two terms is indicated by scaling the single-photoelectron responses by $\sqrt{N_{pe}}$, where N_{pe} is the average number of photoelectrons seen by the PMT of a counter with an infinitely long attenuation length. For scintillators that are several meters long, the dominant contribution comes from transit time variations of photon paths in the scintillator.

The values of the parameters σ_0, σ_1, and σ_2 for the panel-1a and panel-2 counters are given in the CLAS TOF paper [3], where the above functional form with the parameters listed in Table 3 was found to well describe the measured data. A direct extension of these parameters is assumed to be reasonable for

estimating the timing resolution for the panel-1b counters. For the estimates used for the FTOF timing resolutions, the parameters employed are listed in Table 3. Note that due to improvements in the resolution of the readout electronics for the CLAS12 FTOF system compared to the CLAS TOF system, the floor-term σ_0 has been reduced from 62 ps to 40 ps.

Parameter	Nominal Value
σ_0	0.062 ns [CLAS TOF]; 0.040 ns [CLAS12 FTOF]
σ_1	2.1 ns [panel-1a/1b]; 2.0 ns [panel-2]
σ_2	2.0 ns
N_{pe}^0	918
λ	$0.358 \cdot L + 81.725$ cm

Table 3
Parameters determined for the CLAS TOF panel-1a and panel-2 counters in Ref. [3] and used for a parameterization of the CLAS12 FTOF counters using the functional form for σ_{TOF} in Eq.(1) and for N_{pe} in Eq.(2).

The number of photoelectrons N_{pe} in Eq.(1) for panel-1a and panel-2 at the PMT photocathode was determined in Ref. [3] according to:

$$N_{pe} = N_{pe}^0 \exp\left(\frac{L_0}{2\lambda_0} - \frac{L}{2\lambda}\right) \cdot F, \tag{2}$$

where N_{pe} for all counters was referenced to the average value measured for the response of the shortest panel-1a counter N_{pe}^0 of length $L_0 = 32$ cm with attenuation length λ_0. For the panel-2 counters, N_{pe} is further scaled by the factor $F = 0.9$ to account for light collection efficiencies at the end of the larger panel-2 counters with their 3-in PMTs and longer light guides compared to the smaller panel-1a PMTs with their relatively short light guides [3]. For the panel-1b counters, N_{pe} is determined as for panel-1a using Eq.(2) by scaling by the ratio of the widths of the cross sectional areas of the scintillation bars (15 cm x 5 cm vs. 6 cm x 6 cm).

Fig. 8 shows the parameterized resolution for the counters in panel-1a, panel-1b, and panel-2 as a function of counter length. The Forward Detector event reconstruction and particle identification uses timing information from both panel-1a and panel-1b. For tracks that pass through both arrays the combined timing information (described in Section 5.2.8) is used and results in a 20% improvement compared to using the hit information from panel-1b alone.

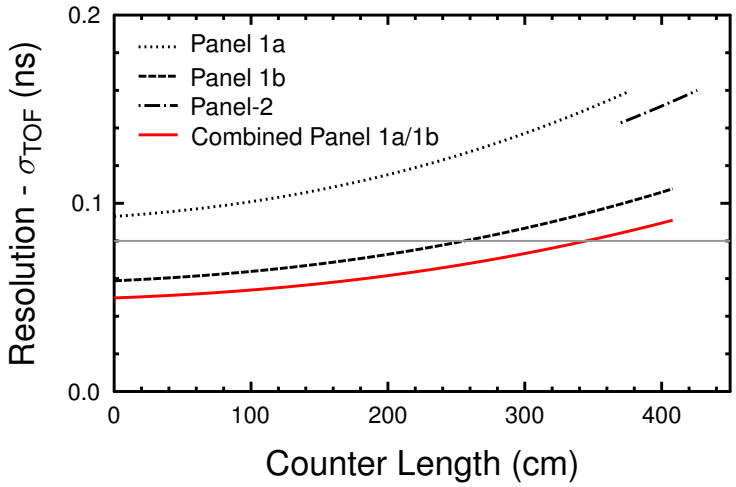

Fig. 8. (Color Online) Parameterized expectation of the counter hit time resolution for the FTOF panel-1a (dotted), panel-1b (dashed), and panel-2 (dot-dashed) counters as a function of length. The solid (red) line indicates the final expected resolution in the forward direction by combining the hit time information from the panel-1a and panel-1b counters. The horizontal line indicates the 80 ps average time resolution specification for the FTOF system.

4.3 System Components

4.3.1 Scintillator Material

To optimize the time resolution over the full volume of the FTOF counters, a scintillation material with a fast time response and a long attenuation length are essential. For the panel-1a and panel-2 FTOF counters that were refurbished from the older CLAS TOF system, Bicron BC-408 was selected. For the panel-1b counters constructed for the new CLAS12 FTOF system, a different design approach was considered that optimized the overall system timing resolution. For counters less than 2 m in length, the overall performance is improved by the use of a faster scintillator with small decay times τ_{decay}, whereas for the longer counters, material with longer attenuation lengths is the better choice. The final decision for the panel-1b counters was to use BC-404 for counters $1 \rightarrow 31$ (lengths from 17.3 cm to 209.4 cm) and to use BC-408 for counters $32 \rightarrow 62$ (lengths from 215.8 cm to 407.9 cm). Table 4 lists the properties of the FTOF scintillation materials.

The bulk attenuation length of the scintillator material is stated by its manufacturer to be 160 cm for BC-404 and 380 cm for BC-408. However, the practical attenuation length of the actual prepared bars is smaller than this bulk value as the real path length of photons from the charged particle intersection point to the ends of the bar is increased due to the finite geometry of the bar. For optimal response, this practical attenuation length should be longer than the bar to ensure sufficient photon statistics. Measurements of the

Property	BC-404	BC-408
Light Output, % Anthracene	68	64
Rise Time (ns)	0.7	0.9
Decay Time (ns)	1.8	2.1
Pulse Width, FWHM (ns)	2.2	2.5
Wavelength of maximum emission (nm)	408	425
Light attenuation length (cm)	140	210
Bulk attenuation length (cm)	160	380
Polymer base	Polyvinyltoluene	
Refractive index	1.58	
Density (g/cm^3)	1.023	

Table 4
The properties of the plastic scintillator material BC-404 and BC-408 employed for the counters of the FTOF system [9].

practical attenuation length of the FTOF counters are given in Section 5.2.2.

4.3.2 Photomultiplier Tubes and Voltage Dividers

The panel-1a counters are read out at either end through 2-in diameter Thorn EMI 9954A PMTs (later manufactured by ElectronTubes) [10]. The PMTs were coupled to the scintillation bars using 12-cm-long Acrylic light guides that matched the 15 cm x 5 cm scintillator on one end and the 2 in diameter PMT on the other end. For the panel-2 counters Philips XP4312B/D1 3-in diameter PMTs (later manufactured by Photonis [11]) are employed. The PMTs were coupled to the scintillators through Acrylic light guides that matched the 22 cm x 5 cm scintillator on one end and to the 3 in diameter PMT on the other end. Both the 9954A and XP4312B/D1 PMTs have 12 linear-focused dynode stages. For both the panel-1a and panel-2 counters the PMTs are glued on the light guides using BC-600 optical glue. See Ref. [3] for full details on the PMT selection criteria and the light guide designs. The performance specifications for these PMTs are listed in Table 5.

The voltage dividers employed for the panel-1a and panel-2 readout were custom units built specifically for the CLAS TOF project [3]. The dividers use high voltage field-effect transistors to fix the PMT gain by stabilizing the voltage and to protect the PMT against high light levels by shutting down the circuit in case of over-current. The grid voltage for both types of dividers followed the manufacturer's specifications.

The photomultipliers employed for the panel-1b counters are Hamamatsu R9779 2-in diameter PMTs integrated with a voltage divider to form the R9779-20MOD assembly. These PMTs include 8 linear-focused dynode stages. This high timing resolution PMT was selected due to its particularly compact overall length of ∼115 mm. The length restriction was necessary to fit within the defined shadow region of the torus cryostats at the location of the PMTs (see Section 4.1 for details). These PMTs are coupled directly to the ends of the scintillation bars using BC-600 optical glue. The performance specifications for these PMTs are listed in Table 5.

	9954A	R9779	XP4312B/D1
Property	Panel-1a	Panel-1b	Panel-2
Diameter	2 in	2 in	3 in
Photocathode area	16.6 cm^2	16.6 cm^2	36.3 cm^2
Dynode stages	12	8	12
Spectral response	290 → 680 nm	300 → 650 nm	290 → 650 nm
Max. wavelength emission	400 nm	420 nm	420 nm
Gain	1.8×10^7	5.0×10^5	3×10^7
Quantum eff. @ λ_{max}	28%	28%	28%
Max. anode current rating	100 μA	100 μA	100 μA
Anode dark current	2 nA	15 nA	10 nA
Anode pulse rise time	2 ns	1.8 ns	2.1 ns
Electron transit time	41 ns	20 ns	31 ns
Transition time spread	0.4 ns	0.25 ns	0.4 ns

Table 5
The properties of the PMTs used for the readout of the FTOF panel-1a, panel-1b, and panel-2 counters. All of these PMTs have a borosilicate glass window and employ green-sensitive bialkali photocathodes.

4.3.3 PMT Magnetic Shielding

The FTOF PMTs are located roughly 600 cm to 700 cm from the target in a local magnetic field from the torus computed to be less than 30 G when the torus is operated at full field. The magnetic shields for the PMTs are included to reduce both the axial and transverse components of the field along the full accelerating structure of the PMT to a level less than 0.2 G. For the panel-1a and panel-2 counters, the PMT magnetic shields consist of a 0.020-in thick μ-metal cylinder, with the shield extending 2-in beyond the front face of the PMT. For the panel-1b counters, the magnetic shields are composed of 2 mm

thick μ-metal that extends 2-in beyond the front face of the PMT. The shield has a rectangular box design that fits over the edge of the scintillation bar. The face of the shield opposite the PMT side has a small penetration to allow the signal and HV cables and connectors to pass through. Further details on the FTOF magnetic shielding and the field tests that were conducted are included in Ref. [12].

4.3.4 Counter Assembly and Support

Each scintillation counter is individually wrapped first with a reflective layer and then an opaque outer layer. For panel-1a and panel-2 the scintillation counter wrapping materials include:

- 1 layer of 0.0094 in (0.02388 cm) thick black Kapton,
- 2 layers of 0.001 in (0.00254 cm) thick aluminum foil,

For panel-1b, the scintillation counter wrapping materials include:

- 3 layers of 0.0015 in (0.00381 cm) thick Tedlar,
- 1 layer of 0.0003 in (0.00076 cm) thick aluminized Polyester film,

After wrapping, each of the FTOF scintillation counters was attached to a support structure that consists of a composite sandwich structure of stainless steel skins on structural foam that is attached to the detector frame only at the two ends. The composite structure, which mounts on the scintillator side facing away from the target, provides uniform material thickness to the scattered particles. The support was undersized so the counters could be placed as close together as allowed by the wrapping material.

Each panel-1a counter was mounted on 1-in-thick supports to minimize the thickness of the package from the standpoint of Coulomb multiple scattering and energy loss considerations. The maximum deflection for the installed scintillators is 4.4 mm, as estimated from deflection tests and the compound angle of each detector, which relieves the overall support requirements. The space for the panel-2 counters allowed for 3-in-thick sandwich supports, which were mechanically much stiffer and resulted in no appreciable deflection. Again, each panel-2 counter was mounted to its own support structure. For the panel-1b counters, the backing structures were 2-in thick and designed to support two panel-1b counters. The maximum deflection for the installed scintillators is less than 5 mm, which occurs at the middle of the longest counters.

The support structures onto which the scintillator counters were attached were bolted to box-beam support frames (steel for panel-1a and panel-2, aluminum for panel-1b) that resided in the torus shadow regions. The support frames were triangular in shape for panel-1a and panel-1b, and formed a rhombus

shape for panel-2. The panel-1a frames were bolted directly to the upstream faces of the electromagnetic calorimeters in each sector of the Forward Carriage. The panel-1b frames were bolted directly to the panel-1a frames. The panel-2 frames were attach to the steel super-structure of the Forward Carriage.

4.4 Electronics

The outputs from the FTOF PMTs include both an anode and a dynode signal. The anode signals are sent first to a discriminator and then to a TDC. The dynode signals are sent to a flash ADC. A block diagram of the electronics layout for each FTOF counter is shown in Fig. 9.

For the FTOF PMTs the anode signal is roughly three times larger in amplitude than the dynode signal. For the panel-1a and panel-2 PMTs, the dynode signals are bipolar with a negative polarity primary pulse with a long tail that overshoots the baseline. This tail is not included in the determination of the pulse charge. For the panel-1b PMTs, the anode signal has negative polarity and the dynode signal has positive polarity. To ensure compatibility with the negative polarity input requirements of the FADC, the dynode signal is inverted before the readout electronics using an inline Philips 460 IT inverting transformer.

The output from the panel-1b FADCs is also used as part of the CLAS12 level-1 trigger. Signals in panel-1b above the FADC threshold are geometrically matched to cluster hits in the electromagnetic calorimeter and to found tracks in the drift chambers to select charged hadrons. Signals from the FTOF system are also used to provide an effective charged particle veto for the detection of neutrals in the electromagnetic calorimeters. While high resolution timing measurements are the primary role of the FTOF system for charged particle identification in the forward direction of CLAS12, the pulse height information from the FADCs is also employed for energy loss measurements to provide an independent means for identification of slow particles. In addition, pulse fitting techniques are employed using the FADC pulse shape to determine the hit time of the track that can be matched to the TDC time to better ensure matching of the ADC and TDC information in the high rate operating environment of CLAS12 (see Section 5.2.8.)

The intrinsic resolution of the electronics system (σ_0) must be reduced in order that it not provide a limitation to the effective counter timing resolution. There are several contributions to this term and each electronic component was studied to understand its effect. From our bench measurements and measurements from CLAS12, a reasonable approximation for the floor term in the

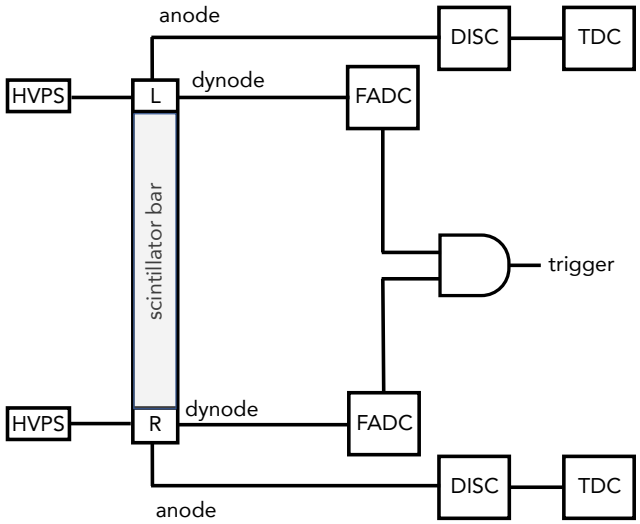

Fig. 9. Schematic of the electronics for each counter in the CLAS12 FTOF system.

counter hit time resolution is $\sigma_0 = 40$ ps (see Section 4.2). The PMT anode outputs are connected to JLab-designed VME leading-edge discriminators. A leading-edge, rather than a constant-fraction, discriminator was chosen for the FTOF system. Although a constant-fraction discriminator delivers better timing initially, off-line time-walk corrections to leading-edge time give comparable results at a significantly lower cost since the off-line analysis can use the measured charge. Time walk is an instrumental shift in the measured hit time that arises due to the finite rise time of the analog pulse. For a given event time, pulses of different amplitude cross the leading edge discriminator at slightly different time. The time-walk correction algorithm is described in Section 5.2.4. The discriminator threshold was set at -25 mV, significantly above the 1-2 mV noise level. This threshold corresponds to $\sim$1 MeV of deposited energy. The discriminator width was set to 35 ns in order to prevent multiple outputs from the same input pulse.

The output of the discriminator goes to a CAEN VME TDC. Both high resolution TDCs (25 ps LSB CAEN VX1290A) and lower resolution TDCs (100 ps LSB CAEN V1190A) are employed [13], where the lower resolution TDCs are associated with the longer counters at large polar angles for panel-1a ($N_{counter} = 17 \rightarrow 23$), panel-1b ($N_{counter} = 49 \rightarrow 62$), and panel-2 ($N_{counter} = 1 \rightarrow 5$). These multi-hit pipeline TDCs were chosen in order to allow for readout capability in the operating luminosity of 10^{35} cm^{-2}s^{-1}. The TDC readout window was set to 250 ns to ensure the full dynamic range of the data was safely in time with the trigger. The key performance specifications of these units are given in Table 6.

The integral non-linearity (INL) of the TDCs represents the accumulated error of the input-output characteristic of the TDC with respect to the ideal

response. This is defined by the function:

$$D(t) = \int \frac{t}{LSB}, \tag{3}$$

where D is the output data, t is the input time, and LSB is the bin size. The compensation tables for the CAEN V1190A and VX1290A TDCs are stored as tables in the unit SRAM memory. Initial tables are measured at the factory and come preloaded on the modules. These tables are reasonably accurate when reading out the module using its internal 40 MHz/25 ns period clock. However, in CLAS12, the modules are strobed with a clock of a slightly larger frequency of 41.67 MHz. This difference in the frequency has a non-negligible affect the INL tables. For our purposes we use a high frequency pulser to populate the full dynamic range of the TDC within the CLAS12 readout clock. The measured INL tables that were derived from this calibration were written into the TDC memory to replace the factory-loaded values. Details on the procedure and the residual non-linearity affects are given in Ref. [14].

The PMT dynode outputs are connected to the FADCs for the pulse charge measurement. The readout employs JLab-designed FADC250 16-channel VME 250 MHz flash ADCs are employed [15]. The JLab-250 FADC units can be operated in several readout modes. For standard data acquisition operation the FTOF counters are readout in a mode where the pedestal is subtracted event-by-event. Fig. 10 shows a raw ADC pulse from a representative FTOF PMT where the pedestal has not been subtracted. Our procedure determines the pedestal over the first 15 channels. This average is subtracted from our pulse signal region, which lies between channels 35 and 65. A pulse fitting algorithm that fits the leading edge of the pulse down to the baseline is used to determine the hit time from the FADC signal. The readout window for the FTOF FADCs is set to 192 samples (48 ns). The applied readout threshold is set to $\sim$1 MeV to ensure that the hit cluster energy can be determined with a reasonable accuracy. Details on the hit clusterization for FTOF are described in Section 5.2.8. The key performance specifications of these units are given in Table 6.

The signal cables used for the FTOF system to connect from the PMT anodes and dynodes to the Forward Carriage patch panels were RG-58C/U fire-retardant coaxial cables. This type of cable is appropriate for moderate length cable runs for fast signals with low signal distortion requirements. The cable runs vary from 47 ft to 59 ft. The connections from the patch panels to the readout electronics were made with a final 5 ft run of low loss RG-174 coaxial cable. The inline signal inverting transformers for the panel-1b dynodes (see Section 4.4) were attached directly to the Forward Carriage patch panels.

TDC Specs (V1190A/VX1290A)	ADC Specs
No. Channels: 128/32	16
RMS resolution 100 ps/25 ps	Sampling 250 MHz
Resolution: 19 bit/21 bit	Resolution: 12-bit
Inter-channel isolation $\leq$ 3 LSB	Clock jitter 350 fs
Double-hit resolution 5 ns	Data memory 8 μs
Full-scale range 52 μs	Trigger/Data latency 8 μs / 32 ns
Integral/Differential non-linearity	
$<$ 2.5 LSB / $<$ 3 LSB	$\pm$0.5 LSB / $\pm$0.8 LSB
Inter-channel isolation $<$ 3 LSB	SNR 56.8 dB @ 100 MHz input

Table 6
The key performance specifications of the FTOF CAEN V1190A and VX1290A pipeline TDCs and JLab FADC250 flash ADCs.

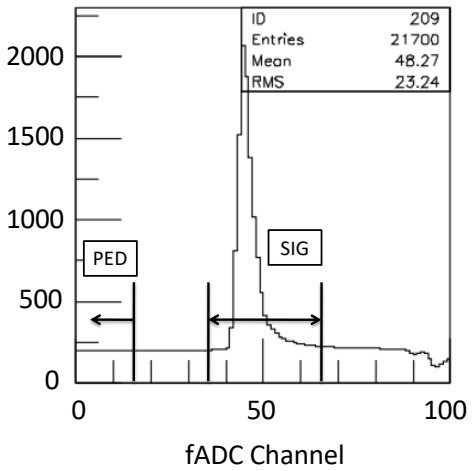

Fig. 10. Typical FADC pulse from a representative FTOF counter with the JLab FADC250. The "PED" region is used to determine the average pedestal in the "SIG" region shown about the PMT pulse.

4.4.1 High-Voltage Supplies

The PMTs for the FTOF counters typically operate at about 2000 V with negative polarity. The typical dark current drawn by the PMTs on the assembled counters was $<$ 20 nA. The system is powered by a single high voltage mainframe for each sector. These mainframes are either CAEN 1527LC or CAEN 4527 units outfitted with negative polarity 24-channel A1535N modules that can supply up to 3.5 kV per channel with a maximum current of 3 mA. The power supply has a voltage ripple specification of $<$20 mV peak-to-peak (typical). Each channel consumes less than 1 W during counter operation. The

typical supply currents per channel are 300 μA to 500 μA.

The mainframe is controlled remotely through the Hall B Slow Controls system. A graphical user interface using EPICS [16] running on a UNIX system communicates with the mainframe via Ethernet. The mainframe settings enable basic protection of the PMTs in terms of maximum voltage and current settings, and channel ramp rates.

The high voltage cables for each PMT are fire-retardant RG-59 coaxial cables that run from the voltage divider to a local disconnect HV distribution box located behind the panel-2 arrays in each sector. There are four HV distribution boxes for each sector, two for the left PMTs and two for the right PMTs of each sector. The output of each HV distribution box is a pair of 35-ft-long multi-conductor cables, each containing 24-channels, with a Radiall connector to mate with the HV A1535N board input connector. The multi-conductor high voltage cables employed each contain 30 conductors wrapped in Tefzel insulation, and outer wire shield and PVC insulation wrap. Each conductor is 5-kV rated.

5 FTOF Performance

This section highlights the performance of the FTOF system both on the test bench and in Hall B during the first beam runs for CLAS12. The bench test timing performance is important to understand to ensure that both the refurbished counters that make up the panel-1a and panel-2 array from the CLAS TOF system still meet their original performance specifications as detailed in Table 1 and Ref. [3]. These bench performance studies are even more important for the newly constructed panel-1b FTOF arrays for CLAS12 as they are primarily responsible for the limits of the particle identification separation for CLAS12 in the forward direction. Full details on the bench test performance results for the panel-1a and panel-2 counters are provided in Ref. [17] and for the panel-1b counters are provided in Ref. [6].

In this section the essential performance results from the bench testing studies in terms of the counter photoelectron statistics and benchmark timing calibrations are presented. Then the nominal algorithms are presented to provide details on how the in-beam FTOF timing resolution performance was calibrated and quantified. Finally, this section provides the current status of the particle identification capabilities of the FTOF system in relation to the design specifications.

5.1 Bench Measurements

5.1.1 Counter Photoelectron Statistics

The primary approach to determine the number of photoelectrons at the photocathode of the PMTs generated by minimum-ionizing particles in the scintillation bars (see Ref. [18] for further details) employs the ratio of the integral of the pulse for a minimum-ionizing particle to the integral of the pulse for a single photoelectron. For these measurements we used the pulse integration feature of an Agilent Technologies MSO-X 3034A 350 MHz (4 GSa/s) oscilloscope and averaged 1000 pulses. The minimum-ionizing particle signals were analyzed connecting the scope to the PMT when mounted in position on the shortest FTOF panel-1a counter. For the single photoelectron signal, we took data using just a bare PMT on the bench using the same gain setting. For both measurements the oscilloscope threshold was adjusted appropriately. For the minimum-ionizing peak analysis the threshold had to be set high enough (>200 mV) to eliminate tracks that did not pass normally through the bar. For the single photoelectron peak the threshold had to be set low enough (1 mV) to pick out the noise pulses that were the source of the PMT intrinsic dark current. This measurement scheme yielded N_{pe}=1000±100. This value is consistent with that found during the initial characterization of these counters for the CLAS TOF system nearly 25 years ago [3]. Based on the parameterization given in Eq.(2), Fig. 11 shows the number of photoelectrons at the PMT photocathodes for the different FTOF counters.

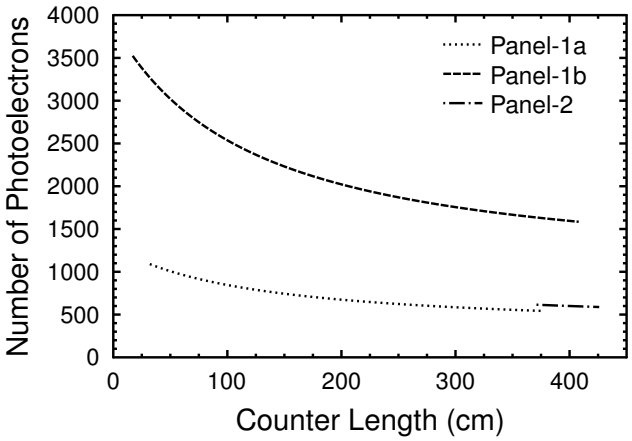

Fig. 11. Parameterized distribution of the number of photoelectrons vs. counter length (cm) in the different panel-1a (dotted), panel-1b (dashed), and panel-2 (dot–dashed) counters based on direct measurements with the shortest panel-1a counter.

A second method to determine the number of photoelectrons produced at the PMT photocathode, which already accounts for the quantum efficiency at the

photocathode, can be estimated from cosmic ray data using the form [19]:

$$\langle N_{phe} \rangle = \left(\frac{M_{ADC}}{\sigma_{ADC}} \right)^2, \tag{4}$$

where M_{ADC} is the ADC mean for the muon peak in the ADC spectrum and σ_{ADC} is the width of the ADC distribution. These quantities are most accurately determined from the system after the PMTs are well gain matched. The form of Eq.(4) assumes that a finite σ_{ADC} arises solely due to statistical variations in the number of photoelectrons created at the photocathode for an event sample with a fixed energy loss per track, which we can assume to be a good approximation for normally incident minimum-ionizing tracks. To determine the average number of photoelectrons based on Eq.(4), it is important that we minimize any attenuation length effects that lead to absorption of the scintillation light as it propagates along the counter toward the PMTs. This can be done by restricting the coordinate along the counter to within ± 5 cm about the center of the bar. From the measured data averaged across the counters in panel-1a and panel-1b it was found that $N_{phe}^{1a} = 373 \pm 39$ and $N_{phe}^{1b} = 1158 \pm 77$ [20]. These results, while roughly a factor of two below the parameterized estimates also show the same factor of three difference in the expected number of photoelectrons for panel-1b relative to panel-1a. The estimates from the first approach are considered more reliable first because they are connected to a more direct measurement of the number of photoelectrons, but also because this parameterization for N_{phe} used in Eq.(1) agrees reasonably well with the measured counter resolutions shown in Section 5.2.7.

5.1.2 Bench Time Resolution Performance

The basic algorithm used on the test bench for the panel-1a and panel-2 counters to determine the time resolution of a given reference counter is to use incident cosmic ray muon tracks to compare the measured time for the reference counter to the time measured by two other identical counters in a triplet counter configuration (see Fig. 12). For a triplet measurement, where the track passes through all three counters with double-sided readout, six times are measured ($t_1 \rightarrow t_6$). Each time measurement actually represents the difference between the discriminated PMT signal (TDC start) and the trigger time (TDC stop from the six PMT coincidence). These timing measurements are then translated into three counter hit times $t_{t,m,b} = \frac{1}{2}(t_{1,3,5} + t_{2,4,6})$.

For incident tracks that pass fully through each counter of the triplet with measured times t_t, t_m, and t_b, we can define a time residual $t_r = t_m - \frac{1}{2}(t_t + t_b)$, where we should expect that the time t_m of the middle scintillator hit should be the average of the measured times t_t and t_b for the top and bottom scintillator hits, respectively. Thus the measured residual t_r should nominally

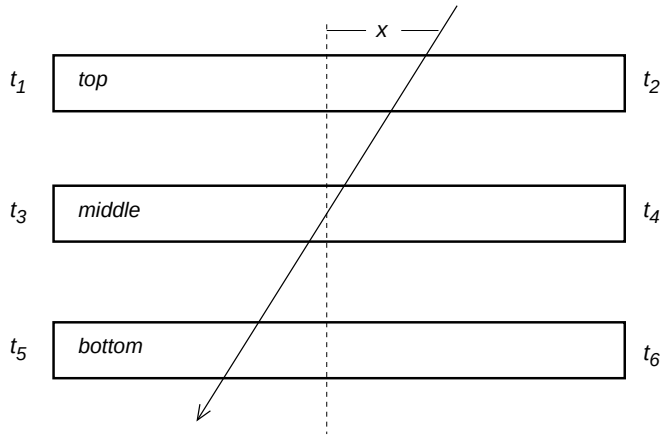

Fig. 12. Schematic representation of a triplet of counters (labeled top - t, middle - m, bottom - b) with a muon track traversing the stack. The geometry of the triplet is configured such that the separation between the top and middle counters matches that of the middle and bottom counters.

be 0. However, due to the smearing of the measured times t_t, t_m, and t_b due to the finite time resolution of the measurements, the residual time t_r will also be smeared. While we still expect the mean of t_r to be zero, the width of the t_r distribution can be used to determine the average time resolution of each counter in the triplet. (For the outer counters in the triplet, the definition of the time residual must be slightly modified to account for the small path length difference between the reference counter and the other two counters.)

The average time resolution of each counter is computed from the variance δt_r in the measured time residual t_r. Assuming the average time resolution for each PMT in the triplet (Δt_i, $i = 1 \rightarrow 6$) is identical and taking into account that each counter is readout using two PMTs, we can write the final expression for the average counter timing resolution as:

$$\sigma_{counter} = \frac{2}{\sqrt{6}} \delta t_r. \tag{5}$$

Thus a measure of the width (σ) of the time residual distribution provides a measure of the average resolution of each counter in the triplet.

Fig. 13 shows the average timing resolution measured for the triplet configurations for the panel-1a and panel-2 FTOF counters. For these measurements the fully assembled counter arrays were stacked one above the other in the cosmic ray test stand. The triplets were formed from the counters for Sectors 1, 6, and 5 and separately for the counters for Sectors 2, 4, and 3. This analysis included a minimum PMT ADC cut to remove events that did not pass through the full thickness of the counter ("corner-clippers") and also included a coordinate cut of ± 10 cm about the center of the scintillation bar.

Due to the use of leading edge discriminators the measured PMT times were corrected with a time-walk function of the form:

$$t_{walk}^{L,R} = \frac{A_0}{1 + A_1\sqrt{(ADC - PED)_{L,R}}}. \quad (6)$$

Here, $ADC - PED$ is the pedestal-subtracted ADC value for each PMT. The time-walk functional in these measurements best described the data using $A_0 = 50.0$ and $A_1 = 0.852$.

The average time resolutions for the counters in the panel-1a S1-S6-S5 and S2-S4-S3 triplets were found to be slightly better (∼15%) than that achieved for the baseline measurements over 20 years ago. For panel-2, the average time resolution was found to be slightly worse (∼15%) than these same baseline measurements.

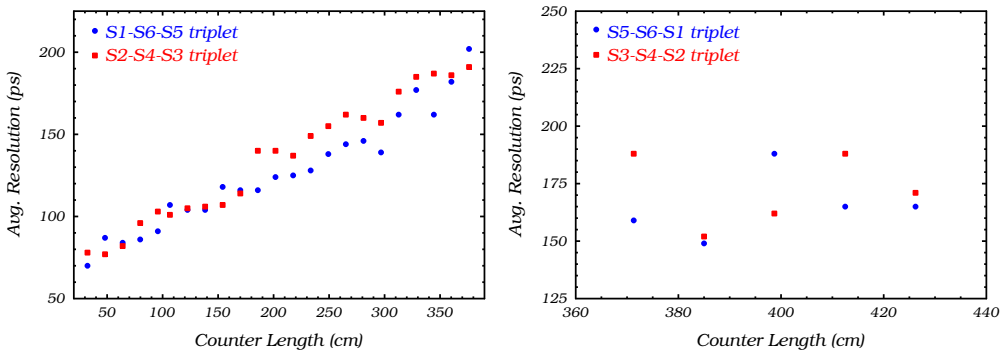

Fig. 13. (Color Online) Average bench measurement resolutions (ps) vs. counter length (cm) using cosmic ray muons for the refurbished FTOF panel-1a (left) and panel-2 (right) counters. The different sets of data points correspond to the two different cosmic ray test stands used for calibration. The data points for the counters in sectors 1, 5, and 6 were averaged together and the data points for the counters in sectors 2, 3, and 4 were averaged together.

The bench measurements for the panel-1b FTOF counters were carried out using a stack of six identical counters from $N_{counter} = 1 \rightarrow 62$. The approach to determine the average time resolution for a given $N_{counter}$ was similar to that for the measurements of the panel-1a and panel-2 triplets. Again, the measured time for a given reference counter in the stack of six counters was compared to the average time measured by the other five. Accounting for the necessary path length corrections to relate the reference counter time to the five-counter average time, a time residual generalized from that in Eq.(1) was employed again assuming that the PMT time resolution was the same for all 12 gain-matched PMTs in the sextet test stand configuration. Also in distinction to the simple time-walk correction employed for the panel-1a and panel-2 measurements shown in Eq.(6), a more sophisticated position-dependent time-walk correction was employed that generalized the simpler

position-independent form. Precision measurements of the time-walk amplitude (A_0 in Eq.(6)) vs. the distance from the PMT showed a nearly linear fall-off of the amplitude with increasing distance from the PMT. On average the time-walk amplitude is ∼30% larger at the PMT compared to the far end of the bar, although this near end to far end ratio of the amplitude decreases linearly with the length of the bar. Our measurements showed this ratio varies between 20% for the shortest bars to 40% for the longest bars. After accounting for this correction vs. hit position along the bar, a final baseline for the average panel-1b time resolutions were extracted averaging over the six identical counters from $N_{counter} = 1 \rightarrow 62$. The final bench measurement results are shown in Fig. 14. The timing resolutions for the panel-1b counters shown in Fig. 14 range from 30 ps for the shortest counters (17 cm long) to 80 ps for the longest counters (408 cm long). Full details describing these measurements are provided in Ref. [6].

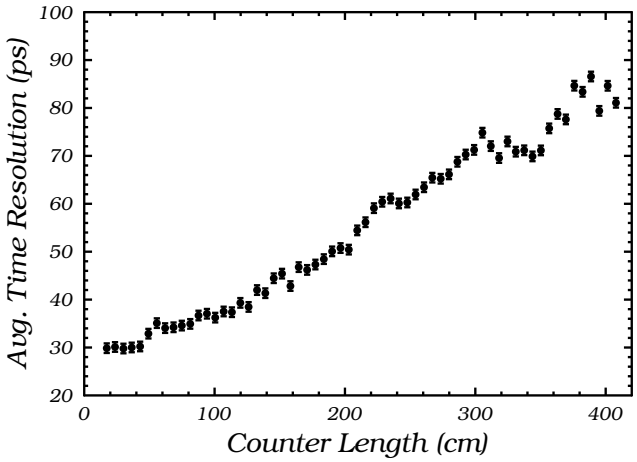

Fig. 14. Measurements of the time resolution (ps) vs. counter length (cm) achieved for the FTOF panel-1b system averaged over the six identical counters belonging to each CLAS12 Forward Carriage sector. These data were acquired on the bench using cosmic ray muons. Full details are included in Ref. [6].

For our purposes in quoting counter time resolution values, it is essential to distinguish between two different quantities. the first is the *intrinsic* counter time resolution that reflects the resolution defined in Eq.(1). This includes the resolution contributions mainly due to photon statistics at the PMT photocathode due to the counter geometry, surface quality, scintillation material and bulk quality, wrapping preparations, etc., the transit time spread of the PMT, and the readout electronics noise (the floor term of the resolution). However, when calibrating the time resolution in situ in Hall B with beam interactions in the experimental target, an *effective* time resolution is extracted that includes not only the intrinsic resolution contributions but also contributions from the angle-dependent uncertainty in the path length determined by the CLAS12 forward tracking system and the resolution spread in the accelerator RF signal that is used as a comparison reference time. The results quoted in this section

represent the intrinsic time resolutions of the counters. The effective in situ time resolutions are discussed in detail and presented in Section 5.2.7.

5.2 FTOF Beam-Data Calibrations

In the nominal data taking mode for CLAS12, whenever the FTOF is involved in an event that triggers the spectrometer, the ADCs and TDCs for all PMTs with a signal above the discriminator threshold are recorded. For the FADCs, the charge of the pulse is integrated over the extent of the pulse region and the pedestal is subtracted event by event as discussed in Section 4.4. For the TDCs the time recorded is relative to the trigger. To determine the flight time of the charged track from the target to the FTOF, the TDC time must be compared to the time of the accelerator radio frequency (RF) pulse relative to the trigger. The RF signal from the accelerator has a period an integer multiple of 2.004 ns. The RF bunch length itself corresponds to a few picoseconds. Although the timing signals are very accurate (with a resolution of <20 ps), the determination of which beam bunch produced a given interaction must be determined by the experiment.

The full calibration of the each of the FTOF counters involves a number of discrete steps that are carried out separately for each of our data runs (where a run typically lasts for about two hours). The calibration constants for each run are stored in the CLAS12 calibration database. The steps to the FTOF calibration are carried out in a particular sequence [21].

(1) Left/right PMT time offsets: This time offset accounts for the difference in the time recorded between the left side and right side PMTs in a given counter due mainly to the different PMT transit times. These time offsets are determined by determining the centroid of the difference between the left/right TDC time difference and the left/right TDC time difference computed using the counter hit point from the drift chamber system divided by the effective speed of light in the counter. These time shifts range between ± 5 ns.
(2) ADC Calibration: Determine the ADC channel to energy deposition calibration factor for each counter using minimum-ionizing events. See Section 5.2.1.
(3) Attenuation Length Calibration: This property of the counter quantifies the light absorption length and is determined by relating the measured ADC as a function of hit coordinate along the bar. See Section 5.2.2.
(4) Effective Velocity Calibration: Determine the effective speed of light propagation along the counter. See Section 5.2.3.
(5) Time-Walk Amplitude Calibration: Compare the measured hit time with respect to the measured ADC to determine the time-walk correction am-

plitudes. See Section 5.2.4.

(6) Counter-to-Counter Time Offset Calibration. In order to measure the absolute flight time of a charged particle from the target to the FTOF counter and to be able to reconstruct exclusive events when hits are associated with multiple FTOF counters, the relative time offsets of each counter relative to all of the other counters in the system need to be determined. This is done in two steps for the FTOF calibration. The first step is to align each track to the RF time, a step that amounts to a precision time alignment in bins of the TDC LSB. The second step is a coarse alignment of each counter time in bins of the RF period T_{RF}. See Section 5.2.5. During this same step the effective counter timing resolutions are extracted. See Section 5.2.7.

(7) TDC Calibration: After calibrating the integral non-linearities of each TDC channel in the system (see Section 4.4), the TDC channel to time calibration is completed using beam events. See Section 5.2.6.

5.2.1 Gain Matching

One of the purposes of gain-matching the FTOF PMTs is to equalize the detector response to tracks that cross the FTOF arrays such that two counters are involved. This is a necessary procedure because each counter must contribute equally to the trigger for a common-threshold discriminator level. Gain matching so that the minimum-ionizing particle response is such that the peak location appears in the same ADC channel for all counters also allows for easier data monitoring during online and offline analysis.

The FTOF PMT high voltage settings were determined using calibration runs employing minimum-ionizing tracks. These minimum-ionizing tracks deposit roughly 10 MeV (12 MeV) as they pass through the 5 cm (6 cm) thick FTOF scintillation bars, as $dE/d\rho x = 2$ MeV/g/cm^2 for minimum-ionizing particles. Normally the high voltage settings are based on runs using cosmic ray muons with the readout based on a calorimeter pixel trigger that effectively selected tracks approximately normal to the face of the FTOF counters in panel-1a and panel-1b. These calibrations can also be carried out using minimum-ionizing tracks from beam data coming from the target. In this case the charge information is scaled by a path length correction given by t/P, where t is the counter thickness and P is the path-length of the track in the counter as determined by extrapolation of the drift chamber track to the location of the FTOF counter.

The energy deposited in the scintillation bars follows a Landau distribution for the minimum-ionizing tracks. The energy deposited is recorded by the ADCs, which show a peak above pedestal for the tracks. Tracks that do not pass through the full counter thickness and non-minimum-ionizing tracks give rise

to a background beneath the Landau peak.

For the HV calibrations, to avoid issues with the attenuation of light for tracks that pass near the ends of the bars and to avoid issues with unbalanced light entering the left and right PMTs, we combine the information from the left and right PMTs to produce an average ADC spectrum for the counter through the quantity known as the ADC geometric mean given by:

$$\overline{ADC} = \sqrt{(ADC - PED)_L \cdot (ADC - PED)_R}. \tag{7}$$

Given the finite dynamic range of the ADC, we have chosen to position the minimum-ionizing muon peak in a particular ADC channel that is different for the panel-1a, panel-1b, and panel-2 counters. For all counters this channel is selected so that it is safely above the pedestal, but leaves sufficient range for the more highly ionizing charged tracks of our typical physics events. To minimize PMT aging effects that result in loss of PMT gain with time due correlated with the total charge collected at the first dynode of the accelerating structure, the PMT gains are set as low as possible.

The position of the muon peak in the ADC spectrum is set by the PMT HV values. For a given scintillation bar, the typical average ADC spectrum appears as shown in Fig. 15. Given that the same channel is chosen to position the minimum-ionizing peak for all counters in a given panel-1a or panel-1b panel, this implies that the PMT gain linearly increase in going from the short bars to the long bars to compensate for the attenuation losses in the longer bars.

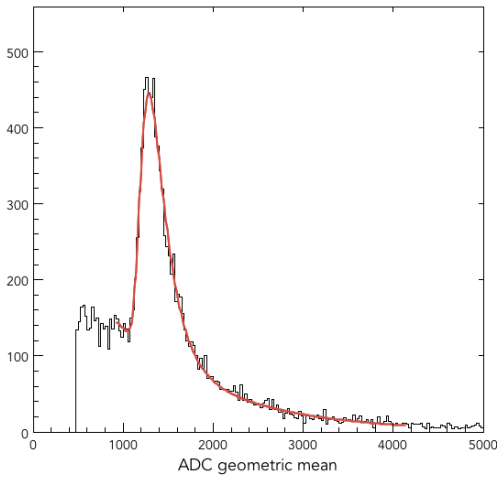

Fig. 15. (Color Online) Geometric ADC mean for one representative FTOF counter from beam data in CLAS12. The events recorded in the ADC spectrum have been pedestal subtracted. The red curve is the fit function that includes a Landau shape for the peak and an exponential for the background.

The PMT gains depend exponentially on the applied voltage. Expressed in a slightly different way, we can relate the PMT gain G_1 at a given voltage V_1 to

the gain G_2 at a different voltage V_2 via:

$$\frac{G_1}{G_2} = \left(\frac{V_1}{V_2}\right)^{\alpha}. \tag{8}$$

This is a basic power law form with α representing the power law factor. Rewriting Eq.(8) in a slightly different form, we have:

$$\frac{\Delta G}{G} = \alpha \frac{\Delta V}{V}. \tag{9}$$

It is this expression that is the basis for relating the position of the muon peak in the $\overline{ADC}$ spectrum (see Eq.(7)) to the PMT HV setting. The gain-matching procedure then amounts to adjusting the HV settings of all PMTs to the values required to position the muon peak for each counter in the desired ADC location. At the same time the algorithm uses the individual left and right PMT ADC spectra for a given counter to ensure that these PMT gains are balanced.

The determination of the power law factor α in Eq.(8) for each PMT type can be determined looking at data with two different high voltage settings. In this manner the average α factors for the FTOF PMTs were determined to be 13.4 for panel-1a, 4.7 for panel-1b, and 8.6 for panel-2. With these values the calibrations converge within just a few iterations such that all of the minimum-ionizing particle peak locations are within $\pm$25 ADC channels of their set targets.

The energy loss in a counter for a passing charged particle track is determined after the minimum-ionizing peak centroids are aligned. The computed energy loss in each counter is computed from each PMT as:

$$E_{L,R} = ADC_{L,R} \cdot \left[\frac{\left(\frac{dE}{dx}\right)_{MIP} \cdot t}{ADC_{MIP}}\right] \exp\left(\frac{d_{L,R}}{\lambda}\right), \tag{10}$$

where ADC_{MIP} is the centroid of the minimum-ionizing peak in the geometric mean distribution, $\left(\frac{dE}{dx}\right)_{MIP}$ is the energy loss for minimum-ionizing particles in the scintillation bars (1.956 MeV/cm), t is the counter thickness (t=5 cm for panel-1a, panel-2, and t=6 cm for panel-1b), d is the distance along the bar from the track hit position to the PMT and λ is the counter attenuation length. The energy loss used in the event reconstruction is the geometric mean of the separate measures $E_{L,R}$.

Fig. 16 shows the reconstructed energy loss normalized by the track path length through the bar for the different counters from a data run with a

10.6 GeV electron incident upon a liquid-hydrogen target. The data allow the separation of minimum-ionizing particles from more heavy ionizing particles. The minimum-ionizing particles lose a constant energy as a function of path length. The heavy ionizing particles have energy loss that increases linearly with distance at low momentum until they can pass through the counter. At that point their energy loss follows the Bethe-Bloch formula.

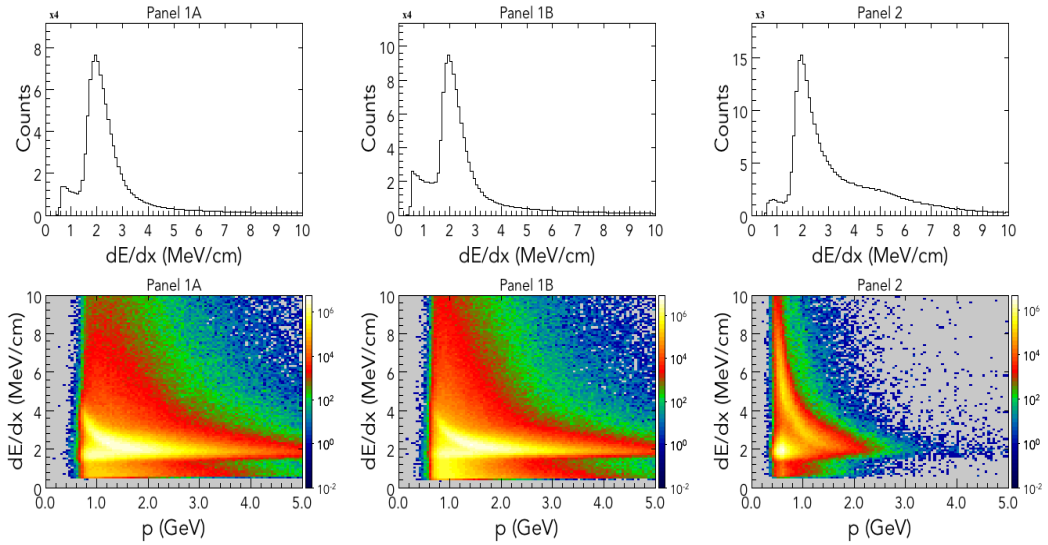

Fig. 16. (Color Online) Measured FTOF counter energy loss for positively charged particles from 10.6 GeV electrons incident on a liquid-hydrogen target normalized by the extrapolated path length from the projection of the forward track through the counter array. This dE/dx (MeV/cm) shows separation of minimum-ionizing particles against more heavily ionizing particles summed over the counters in panel-1a (left), panel-1b (middle), and panel-2 (left). The top row of plots show the measured dE/dx and the bottom row of plots show dE/dx vs. track momentum (GeV).

5.2.2 Attenuation Length Measurements

The attenuation length of the scintillation bars represents the distance λ into the material where the probability that the photon has been absorbed is $1/e$. The measured ADC values for each PMT can be written in terms of the attenuation length as:

$$ADC = A_0 e^{\pm x/\lambda}, \tag{11}$$

where A_0 is a constant, x is the distance along the counter with respect to the PMT location, and λ is the counter attenuation length. Forming this ratio from the ADC values from the left and right ends of the counter,

$$\log\left(\frac{(ADC-PED)_R}{(ADC-PED)_L}\right) = C + \frac{2x}{\lambda}. \tag{12}$$

A linear fit of the ADC log ratio vs. coordinate can be used to extract the effective counter attenuation length.

Fig. 17 shows the measured attenuation lengths for the FTOF counters in one sector of the CLAS12 Forward Detector extracted from data with a 10.6 GeV electron beam incident on a liquid-hydrogen target.

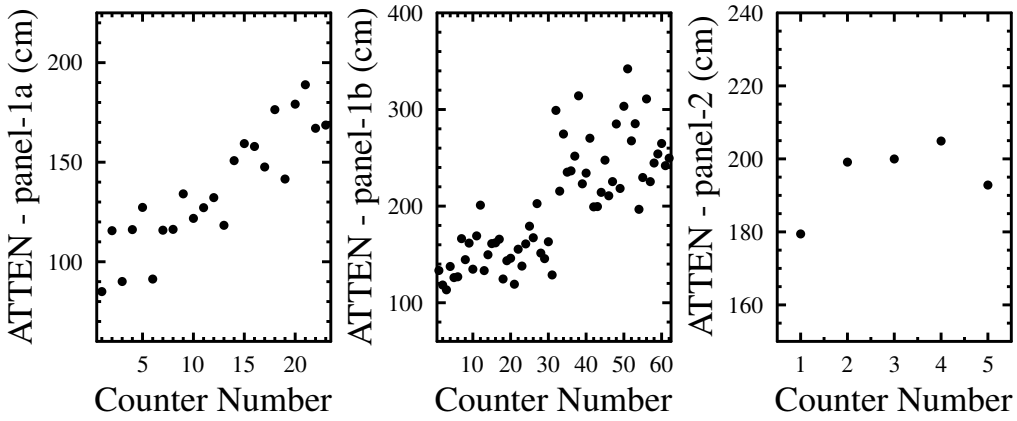

Fig. 17. Counter attenuation lengths (cm) vs. counter number for all FTOF counters in one sector of the CLAS12 Forward Detector determined from beam data.

5.2.3 Effective Velocity Determination

The effective velocity of light in each counter employs a calculation based comparing the reconstructed coordinate information along the scintillation bar from the timing information and from the track hit coordinate determined from extrapolation of the track beyond the drift chambers to the location of the FTOF counters. Fig. 18 shows the measured effective velocity for each counter in one sector of the CLAS12 Forward Detector using data with a 10.6 GeV electron beam incident on a liquid-hydrogen target.

As the counter length increases, so does the effective velocity because light rays at large angles with longer actual trajectories to the PMT are systematically lost owing to attenuation. These constants are used in FTOF analysis to determine the hit time for each event from the measured TDC times. The intrinsic position resolution is given by $v_{eff} \times \sigma(t_L - t_R)$ for each counter, which is most relevant for the interactions of neutral particles. The position for charged particles can be measured more precisely with the drift chambers.

5.2.4 Time-Walk Corrections

The approach that we adopted to correct the FTOF TDC times for time-walk effects is different than was employed for our bench test studies of the counters in their cosmic ray test stands described in Section 5.1.2. We ultimately settled

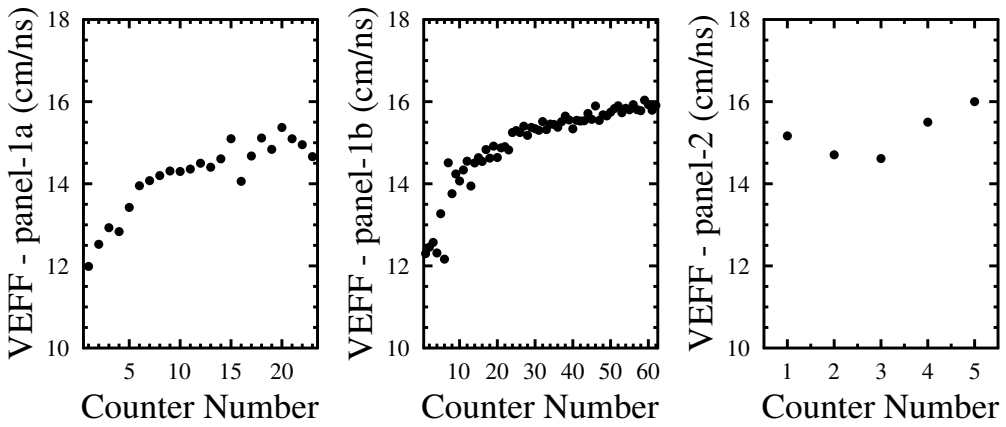

Fig. 18. Counter effective velocities (cm/ns) vs. counter number for all FTOF counters in one sector of the CLAS12 Forward Carriage determined from beam data.

on an approach that first accounts for the average hit position independent correction with a time-walk functional of the form:

$$t^{corr}_{L,R} = t_{L,R} - \frac{tw0_{L,R}}{\sqrt{(ADC - PED)_{L,R}}}. \tag{13}$$

The time-walk amplitude A_0 is determined by defining the following vertex time residual for each PMT:

$$t^{res}_{L,R} = \left(t_{L,R} - \frac{d^{DC}_{L,R}}{v_{eff}} - \frac{L}{\beta c}\right) - \left(t_{RF} + \frac{z_{vert}}{\beta_e c}\right), \tag{14}$$

where $t_{L,R}$ are the measured TDC times after the left/right PMT time offset determination, d^{DC}/v_{eff} corrects the time measured at the PMT to the time of the track hit point on the counter determined from DC tracking information, $L/(\beta c)$ is the track flight time from the reaction vertex to the FTOF. The track path length L comes from DC tracking and β is determined from the FTOF timing and the DC path length, with the particle identification determined from the Event Builder. The term $z_{vert}/(\beta_e c)$ is a term to correct the RF time t_{RF} to account for the actual electron beam event vertex location along the z-axis of the extended target (hence the use of $\beta = \beta_e$)yy. In this expression, $d^{DC}_{L,R}$ are the distances along the bar from the track hit point to the left and right PMTs. This expression represents the FTOF hit time from a single PMT traced back to the reaction vertex and compared to a precise time reference given by the RF signal from the accelerator. As this t_{RF} represents a reference time for the arrival of the electron beam bunch at a fixed position along the beamline in Hall B assigned as the center of the target, the time must be corrected for the displacement of the reaction vertex along the length of the hydrogen target.

As the beam bucket that was associated with the event is not determined

at this point, the time walk for each PMT is actually determined using the modulus of $t^{res}_{L,R}$ with the RF beam bucket period T_{RF} =1/(RF frequency) by fitting:

$$t'_{L,R} = mod(t^{res}_{L,R}, T_{RF}) \text{ vs. } (ADC - PED)_{L,R}. \quad (15)$$

Fig. 19 shows the t' vs. ADC distribution for a representative FTOF PMT in panel-1b from beam data using a 10.6 GeV electron beam incident upon a liquid-hydrogen target. Note that all distributions that employ $t'_{L,R}$ are sorted in 25 ps bins (consistent with the TDC LSB). The overall scale of the time-walk effects spanning the full dynamic range of the ADC is ∼2 ns.

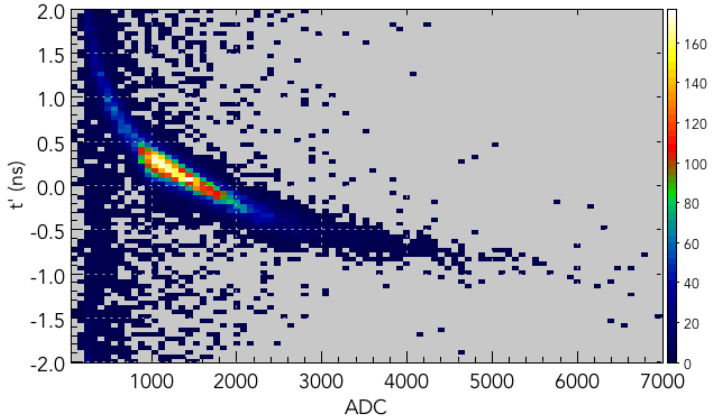

Fig. 19. (Color Online) Plot of t' (ns) vs. ADC for one representative PMT from panel-1b from beam data. As t' is defined using the modulus of T_{RF}, its limits span $\pm T_{RF}/2$.

The second part of the full time-walk correction accounts for the important position-dependence of the effect as discussed in Section 5.1.2. To simplify the algorithm the approach we take is to determine the position-independent correction first for the left-side and the right-side counter PMTs. In a second step we then fit a second-order polynomial to the counter hit time vs. hit position along the counter. Fig. 20 shows the distribution before and after the correction. The time employed for this step is the track hit time at the vertex (relative to the vertex-corrected RF time) averaging the left and right PMT hit times. The before distributions reveal a characteristic "smile" pattern after the position-independent time-walk correction is made. This reflects the convolution of the unaccounted for position-dependent time-walk effects on the measured times incorporating both the left and right PMTs each with their own linearly falling time-walk amplitude moving away from the PMT as discussed in Section 5.1.2. Effectively this approach actually accounts for all remaining position dependence in the calibration parameters. Specifically it should be the case that the effective velocity changes with position along the bar moving away from the PMT. However, the dominant position-dependent parameter accounted for here is the time-walk amplitude.

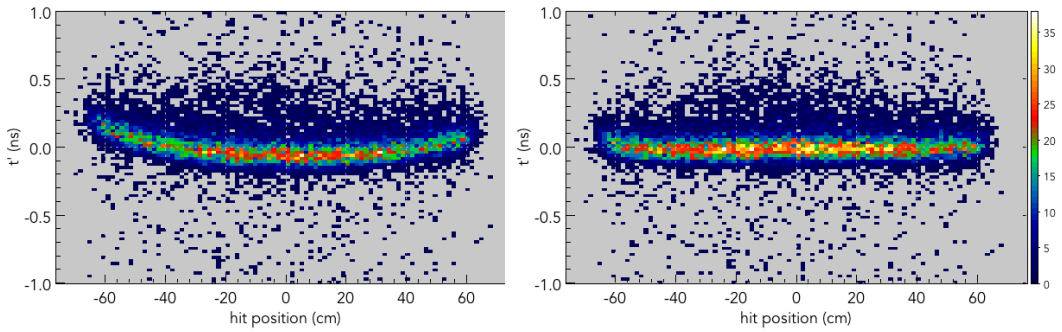

Fig. 20. (Color Online) Plot of t' (ns) vs. hit position (cm) along the bar from beam data after the position-independent time-walk correction (left) and after the ad hoc second-order polynomial fit to remove the residual coordinate dependence (right).

5.2.5 Counter-to-Counter Time Alignment

The flight time of a charged particle from the reaction vertex to an FTOF counter is given by:

$$TOF = \bar{t}_{hit} - t_{ST}, \tag{16}$$

where $\bar{t}_{hit}$ is the average FTOF counter hit time and t_{ST} is the event start time. The event start time is associated with the RF but needs to be synchronized with the particular RF beam bucket associated with the event. The beam bunch width within the RF beam bucket is only ∼2 ps and, therefore, represents a precise time marker. However, as the RF time signal has a period of T_{RF}, it is not initially known which RF beam bucket was the one associated with the event that led to the hits in the FTOF counter.

The determination of the absolute flight time of charged particle tracks from the reaction vertex to the FTOF counters is performed in two steps. In the first step, fine timing offsets (binned in the LSB of the TDCs = 25 ps) are determined to align the FTOF hit times traced back to the vertex for each counter within the RF time window. In the second step, coarse timing offsets binned in units of the RF period T_{RF} are determined to fix the specific RF beam bucket associated with the event.

The fine timing alignment algorithm uses the FTOF hit time traced to the event vertex relative to the RF to align the vertex times of all FTOF hits (modulo T_{RF}). However, instead of using the separate left and right PMT hit times as in Eq.(14), this algorithm uses the average counter hit times,

$$t'_{res} = mod\left[\left(\left(\bar{t}_{hit} - \frac{L}{\beta c}\right) - \left(t_{RF} + \frac{z_{vert}}{\beta_e c}\right)\right), T_{RF}\right]. \tag{17}$$

Fig. 21 shows the t'_{res} distribution for one representative FTOF counter. The

centroid of the Gaussian fit gives the fine timing offset. The width of the Gaussian fit represents a measure of the effective timing resolution of the counter. To display the full t'_{res} distribution avoiding any wrap-around effects near the edges of the T_{RF} range, the algorithm plots the t'_{res} distribution in a range of $\pm T_{RF}/2$ about the peak channel in the distribution.

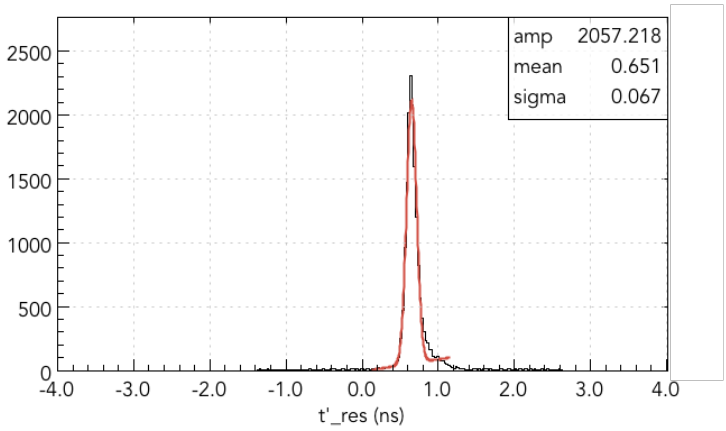

Fig. 21. (Color Online) Distribution of the FTOF hit times from beam data traced back to the vertex relative to the RF (ns) for one representative FTOF panel-1b counter with the Gaussian plus background fit overlaid to determine the counter RF offset and the effective counter timing resolution. As t' is defined using the modulus of T_{RF} this distribution is limited to span $\pm T_{RF}$.

After the fine timing offset calibration, the counter timing is precisely aligned modulo T_{RF}. The next step in the FTOF timing calibration is to fix the measured hit times for all counters to the specific RF bunch associated with the event. This is carried out using coincidences of charged particle tracks to link the hit times of all counters across the full FTOF system.

The coarse timing offset algorithm (called P2P for paddle-to-paddle) selects events with two forward-going charged tracks and for each FTOF counter computes the vertex time difference for a given FTOF counter relative to hits in all of the other FTOF counters,

$$t_{P2P} = t^1_{vert} - t^2_{vert}, \tag{18}$$

where,

$$t^i_{vert} = \overline{t}^i_{hit} - \frac{L}{\beta c}. \tag{19}$$

At this point the counter times have already been aligned to within a multiple of T_{RF}. Note that particle identification of each track is given by the Event Builder, and as both tracks are assumed to originate from the same reaction vertex, no vertex time corrections are necessary. The algorithm adjusts the

vertex time differences over all counters to set them to zero. The coarse time offsets represents a single parameter for each counter that is restricted to values of $n \cdot T_{RF}$, with $n = 0, \pm 1, \pm 2, ...$

Fig. 22 shows the t_{P2P} distribution for one representative FTOF counter before and after the coarse timing alignment. As expected, the histogram is dominated by events in a single channel (of width T_{RF}) centered about $T_{RF} = 0$. As these constants are predominantly determined by the fixed system cable lengths, of which there are four different lengths used to connect the panel-1a and the panel-1b counters, the constants primarily reflect the differences in the signal propagation times along the signal cables. Note that the algorithm specifically identifies two track events for the calibration and does not consider hits in panel-1b and panel-1a associated with the same track.

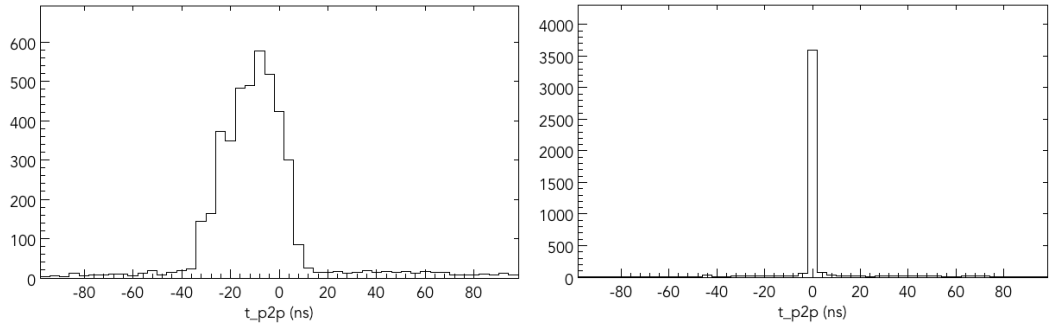

Fig. 22. Distribution of the vertex time differences (ns) for tracks in a single representative FTOF counter compared to tracks in all other FTOF counters using event samples with two forward-going charged particle tracks. (Left) Before P2P corrections, (right) After P2P corrections. The histogram is sorted in bins of T_{RF}.

5.2.6 TDC Calibration

The final calibration step is the calibration of the TDCs. This calibration is a single constant for each TDC channel in the system that converts the measured TDC channel bin into time. The nominal TDC LSB is 25 ps for the CAEN VX1290A and V1190A TDC units employed for the FTOF readout (see Section 4.4).

The calibration is completed by fitting the PMT time residuals of Eq.(14) vs. TDC channel using a linear function. The TDC calibration is the value that fixes the slope of t'_{res} to be zero. Fig. 23 shows the distribution of t'_{res} vs. TDC for a representative FTOF counter. Any bin-to-bin Δt variations reflect remaining integral non-linearities in the measured TDC compensation tables (see Section 4.4). At the present time a single conversion constant of 23.45 ps/channel is employed for the FTOF system TDCs.

The CAEN TDCs used for the FTOF are readout with a 24 ns clock strobed

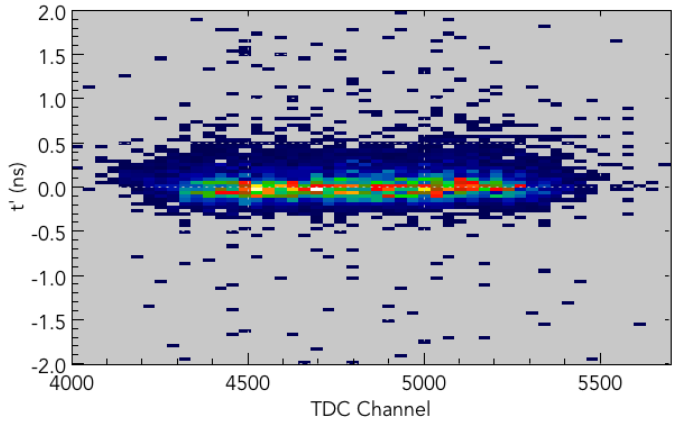

Fig. 23. (Color Online) Distribution of t'_{res} (ns) vs. TDC channel for one representative FTOF panel-1b PMT. The TDC conversion constant for each channel is that which forces the slope of a linear fit to be zero.

so that all TDC times are referenced to an edge of this clock. The CLAS12 trigger comes on the edge of a clock with a period of 4 ns and the TDC stop will not occur until the next 24 ns clock edge. The use of these two different clocks introduces a delay between the trigger and the TDC stop given by $n \cdot 4$ ns, with $n = 0 \rightarrow 5$ (referred to as the six-fold TDC cycle ambiguity) where n is the phase. A TDC jitter correction is made to define the value of the phase n that is valid for the entire data run.

The average hit time resolution for the FTOF from the TDCs is ∼80 ps and that from the FTOF FADCs given the rapid fall time of the fast PMT signals that provide for only 2-3 samples on the falling edge is only ∼1 ns. A matching requirement of 10 ns between the TDC time and the FADC time is employed during event reconstruction. While this matching requirement still needs to be tuned further, at the current time is reasonably efficient at allowing the FADC hits to be matched with the TDC hits. This is important as due to the different thresholds on the discriminators and the FADCs, the number of entries in the hits lists are up to a factor of two different. The matching criteria is also essential in order to assign the correct ADC information to the hit not only for the time-walk correction that directly uses the measured ADC but also for the energy loss computation.

5.2.7 Counter Time Resolutions

The effective time resolutions for each counter determined during the fine timing alignment step discussed in Section 5.2.5 are shown in Fig. 24. These measurements were taken after complete calibrations of the FTOF system from a beam data run with 10.6 GeV electrons incident on a liquid-hydrogen target. The time resolution displayed here represents the quality of the overall CLAS12 calibrations at the current time. The results are based on calibration

procedures that are not yet fully optimized, as well as uncertainties in the reconstructed momentum and path length from the forward track reconstruction. Note that the time resolution floor-term σ_0 discussed in Section 4.2 and Eq.(1) does not include the contributions from the reconstructed path length uncertainties. These uncertainties are polar and azimuthal angle dependent. Near the torus coils the true magnetic field has different variations than accounted for in our conductor model used to generate the field for the event reconstruction. As well, the path length uncertainties grow strongly for high momentum tracks at small angles, which represent the dominant part of our kinematic phase space at 10.6 GeV. It is also important to mention that studies of the CLAS12 subsystem detector alignment based on survey data and based on zero-field straight track data are in progress. Misalignments of the detector affect the quality and accuracy of the reconstruction. When these are accounted for their contribution to the floor-term of the resolution function is reduced.

Nevertheless the time resolutions already achieved meet the system design specifications outlined in Section 3 and shown in Table 1. With these resolutions, the quality of the particle identification in the Forward Detector of CLAS12 allows the experimental program in Hall B to reach its goals. As further operating experience with CLAS12 is gained, we expect to realize further modest but important improvements in the FTOF timing resolution that will allow π/K, π/p, and K/p separation in the Forward Detector of CLAS12 to be pushed to higher momenta than currently seen.

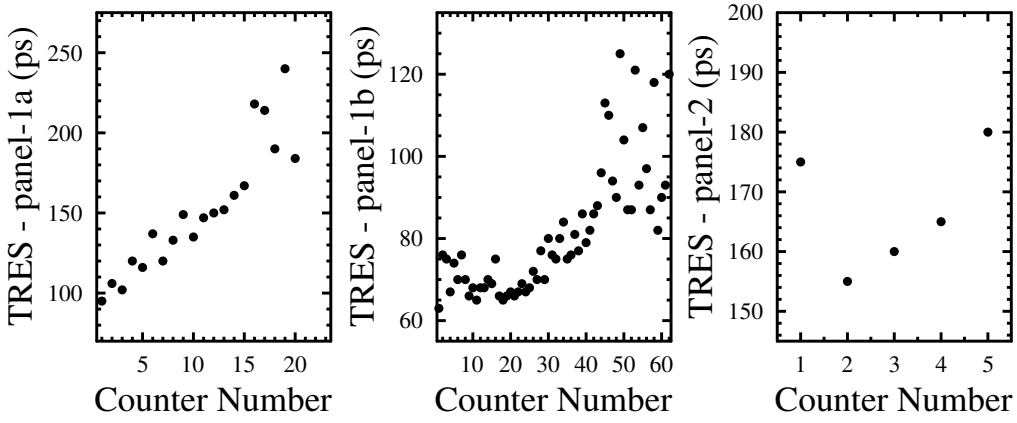

Fig. 24. The measured effective time resolution (ps) vs. counter number for each of the FTOF counters in sector 1 as determined using final state leptons and pions.

5.2.8 Hit Clusterization and Hit Times

The reconstructed FTOF counter hit times need to account for the time delays along the readout path that include the PMT and voltage divider signal transit times, the signal propagation times along the signal cables and the electronics, and the time-walk effects associated with the use of leading edge

discriminators for the readout. Full details on the FTOF reconstruction in terms of reconstructed hit times and energy, the reconstruction algorithm, the time, energy, and coordinate uncertainties, and the hit clustering and matching algorithms are provided in Ref. [22].

The track hit times reconstructed from the readout of the left and right PMTs are given by:

$$t_{L,R} = (C_{TDC} \cdot TDC_{L,R}) - t^{walk}_{L,R} \mp \frac{C_{LR}}{2} + C_{RF} + C_{p2p}, \tag{20}$$

where C_{TDC} is the TDC channel to time conversion factor, TDC is the measured TDC value relative to the trigger signal, t^{walk} is the time-walk correction, C_{LR} is the time shift to center the TDC difference distribution relative to the track coordinate about 0, and C_{RF} and C_{p2p} are the time shifts to align all of the counter times with respect to the RF and to each other, respectively.

The hit times of the passing charged particle relative to the trigger signal can be determined separately from the times t_L and t_R measured by the left and right PMTs, respectively, and are given by:

$$t^{L,R}_{hit} = t_{L,R} - \frac{d^{DC}_{L,R}}{v_{eff}}. \tag{21}$$

where $d^{DC}_{L,R}$ are the distances from the track hit point along the bar relative to the end of the bar as determined by the drift chamber tracking information. The average FTOF hit time is then given by:

$$\bar{t}_{hit} = \frac{1}{2}(t^{L}_{hit} + t^{R}_{hit}) = \frac{1}{2}\left[t_L + t_R - \frac{L}{v_{eff}}\right]. \tag{22}$$

Particle trajectories from the target passing through the plane of a given counter array (i.e. panel-1a, panel-1b, or panel-2) can pass through up to two adjacent counters. To determine the full deposited energy in a given counter layer, a clusterization algorithm is used to match the FTOF counter hits with the track trajectory at the location of the FTOF array. Neighboring FTOF hits that match to the trajectory are assigned to be part of a cluster. The assigned cluster energy is then the sum of the deposited energy in both counters,

$$E_{cluster} = \sum_{i=1}^{2} E^{i}_{dep}. \tag{23}$$

The relevant path length through the layer is then determined from ray tracing of the drift chamber track. This path length through the layer is then used to

compute dE/dx.

The hit time associated with the cluster in a given layer is based on an energy deposition weighted average accounting for the time offset between the cluster hits. For the FTOF reconstruction the assigned hit position in the counter is based on ray tracing of the charged track through the FTOF array. For each counter the hit position is assigned as mid-way between the track entrance point and exit point on the bar. In this way a cluster hit time is computed as:

$$t_{hit} = t_i \cdot \frac{E_i}{E_{tot}} + \left(t_{i+1} - \frac{\Delta r_C}{\beta c} \right), \cdot \frac{E_{i+1}}{E_{tot}} \tag{24}$$

where βc is the track speed and Δr_C is the distance between the hit positions assigned for each of the counters in the cluster.

In the forward direction where there is a defined hit or a defined cluster in both panel-1b and panel-1a, a cluster matching algorithm is applied to determine if the hit or cluster in panel-1b and the hit or cluster in panel-1a are associated with the same incident track. Once the clusters in panel-1b and panel-1a arrays are matched together as associated with the same incident track, the corrected FTOF time based on the panel-1a and panel-1b cluster times is computed using a time resolution weighting based on the counter in each cluster with the largest energy deposition.

$$t_{corr} = \frac{\dfrac{t_{1b}^{cluster}}{\delta_{1b}} + \dfrac{(t_{1a}^{cluster} - \Delta r/\beta c)}{\delta_{1a}}}{\left(\dfrac{1}{\delta_{1b}} + \dfrac{1}{\delta_{1a}} \right)}, \tag{25}$$

Here $\delta_{1a,1b}$ are the time resolutions measured for the counters determined during the fine timing algorithm step (see Section 5.2.5), and $t_{1a,1b}^{cluster}$ are the cluster times defined with respect to the RF time. The term $\Delta r/(\beta c)$ accounts for the path length difference between the panel-1b cluster hit coordinate and the panel-1a cluster hit coordinate and comes from forward tracking information. As β depends on FTOF timing, it is assumed that it is based on panel-1b timing information.

Given the effective FTOF counter resolutions shown in Fig. 5.2.7, the overall FTOF hit time resolution is improved by 20% when combining the times from panel-1b and panel-1a in this manner. Of course if the track interacts with only panel-1a or with only panel-1b due to the slightly different solid angles of coverage of the arrays, then only the single plane hit time is used in the event reconstruction. This is also accounted for in the CLAS12 Monte Carlo simulation code.

5.3 Beam Performance

The first in-beam characterization of the FTOF system took place during the Dec. 2017 to Feb. 2018 CLAS12 Engineering Run and subsequently during the first physics production running period that took place from Mar. - May 2018. During these periods the performance of the FTOF system was tested at different beam energies (2.2, 6.4, 10.6 GeV), different torus and solenoid magnetic field strengths and polarities (from 0 field to full field for both magnets), and over a range of beam-target luminosities up to twice the nominal planned CLAS12 luminosity of 1×10^{35} cm^{-2}s^{-1}. In this section the measured scaler rates and PMT currents as a function of beam current are presented, as well as the reconstruction results and particle identification capabilities relative to the system specifications based on the current system calibrations.

5.3.1 FTOF Rates and PMT Currents

The counting rates during beam operations can be viewed during data taking using the scalers associated with the discriminators or with the FADCs. The threshold applied for these scalers are set at $\sim$1 MeV. During a beam current scan with a 10.6 GeV electron beam incident upon the 5 cm long liquid-hydrogen target from 5 nA to 70 nA (corresponding to the nominal design luminosity for CLAS12 1×10^{35} cm^{-2}s^{-1}) the average counting rate in the different FTOF counters was studied. Averaged over the three different arrays, the results shown in Fig. 25, display a reasonably linear behavior. The rates in panel-1a are about a factor of two larger than those for panel-1b. This is in agreement with the fact that the panel-1a arrays are 2.5 times wider than the panel-1b arrays. However, some portion of the incident radiation is absorbed in the panel-1b counters reducing the flux seen in panel-1a. At the nominal luminosity of CLAS12 the average measured rates in the panel-1b counters are $\sim$500 kHz and those in panel-1a are $\sim$1 MHz.

Based on a detailed simulation of the full CLAS12 detector and beamline based on our GEANT-4 Monte Carlo [23], the response of the FTOF with an 11 GeV electron beam incident upon a 5 cm liquid-hydrogen target has been studied. Shown in Fig. 26 is a comparison of the contributions to the overall rate associated with hits above the readout threshold separated into contributions from photons, neutrons, and charged hadrons. By far the dominant contribution to the overall measured FTOF rate is associated with low energy photons whose energy deposition in the counters is significantly less than the contribution from minimum-ionizing hadrons.

The average PMT current is directly proportional to the average number of photoelectrons $\langle N_{phe} \rangle$ created at the photocathode by the scintillation light

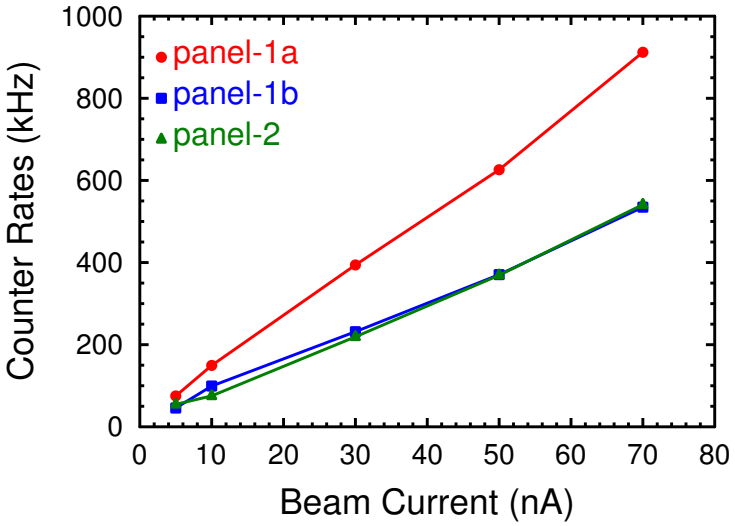

Fig. 25. (Color Online) FTOF counter rates (kHz) for 11 GeV electrons on a liquid-hydrogen target as a function of beam current (nA). The nominal operating luminosity of CLAS12 of 1×10^{35} cm^{-2}s^{-1} corresponds to a beam current of ∼70 nA. The red circles correspond to the average panel-1a counter rates, the blue squares correspond to the average panel-1b counter rates, and the green triangles correspond to the average panel-2 counter rates.

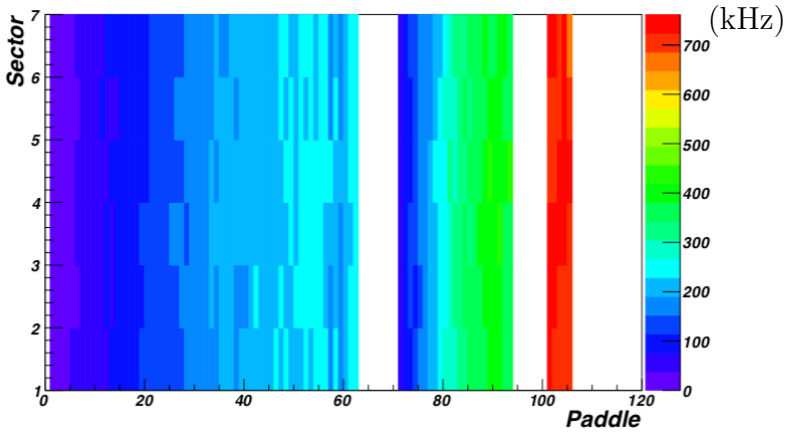

Fig. 26. (Color Online) Simulation results for the FTOF counter rates (kHz) for 11 GeV electrons on a liquid-hydrogen target at the nominal CLAS12 design luminosity of 1×10^{35} cm^{-2}s^{-1}. The rates are calculated for a 1 MeV threshold on deposited energy and expressed in kHz. Here the leftmost group of 62 paddles corresponds to panel-1b, the middle group of 23 paddles corresponds to panel-1a, and the rightmost group of 5 paddles corresponds to panel-2.

and the average incident charged particle event rate $\langle R \rangle$. This current can be expressed as:

$$\langle i_{PMT} \rangle = \langle N_{phe} \rangle \cdot Q_e \cdot G \cdot \langle R \rangle, \tag{26}$$

where $Q_e = 1.6 \times 10^{-19}$ C/e is the electron charge, G is the PMT gain (assumed to be 1×10^6, and R is the rate per bar. Using the photoelectron statistics estimated detailed in Section 4.2, Fig. 27 shows the predictions of the PMT anode currents for all of the FTOF counters at nominal operating luminosity at 11 GeV from our detailed GEANT-4 Monte Carlo studies [24]. These predictions show typical PMT anode currents in the panel-1a and panel-1b PMTs at the level of 5 μA to 10 μA increasing linearly with counter length. Direct measurements in beam of the PMT anode currents were made as shown in Fig. 28. The measurements from beam are in very good accord with the simulation expectations.

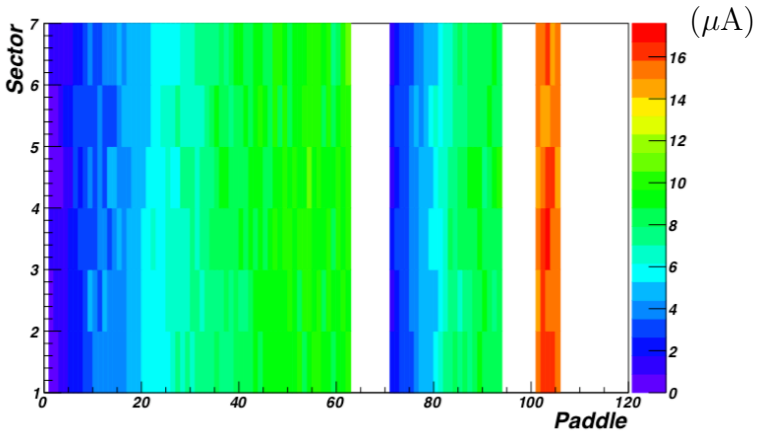

Fig. 27. (Color Online) Computed PMT currents from Monte Carlo studies at the nominal operating luminosity of CLAS12 of 1×10^{35} cm^{-2}s^{-1} with 11 GeV electrons incident upon a liquid-hydrogen target. Here the leftmost group of 62 paddles corresponds to panel-1b, the middle group of 23 paddles corresponds to panel-1a, and the rightmost group of 5 paddles corresponds to panel-2.

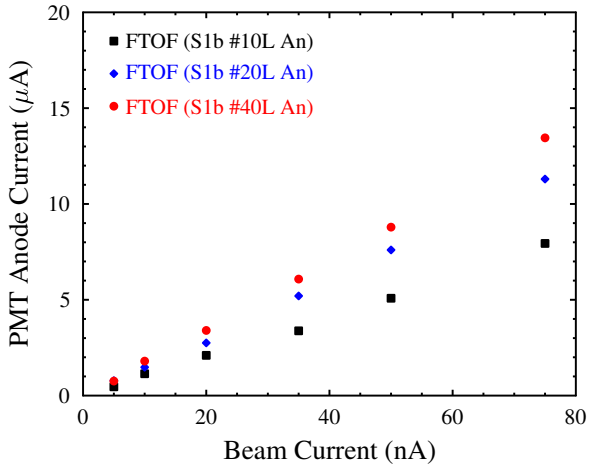

Fig. 28. (Color Online) Measurements of the PMT anode current for representative panel-1b PMTs ($N_{counter} = 10, 20, 40$) as a function of beam current with a 10.6 GeV electron incident upon a 5 cm liquid-hydrogen target.

5.3.2 Reconstruction Results

Particle identification in the Forward Detector of CLAS12 relies heavily on the combination of measured charged particle momenta and the flight time from the target to the respective FTOF counters. The vertex time is determined with respect to the accelerator RF, modulo the RF period T_{RF}. The beam bucket for each event is identified using the flight time of scattered electrons or high-momentum pions, traced back to the interaction point. The FTOF resolution of < 200 ps allows clear selection of the correct beam bucket. In Fig. 29 we show the distribution of masses for all reconstructed positively charged hadrons without any kinematic cuts other than those imposed by the detector acceptance for the data taken with a 10.6 GeV electron beam incident upon a liquid-hydrogen target and after initial calibrations of the FTOF system. A clear separation of pions and protons can be seen from these data. For these data the *RF* period was 4.008 ns.

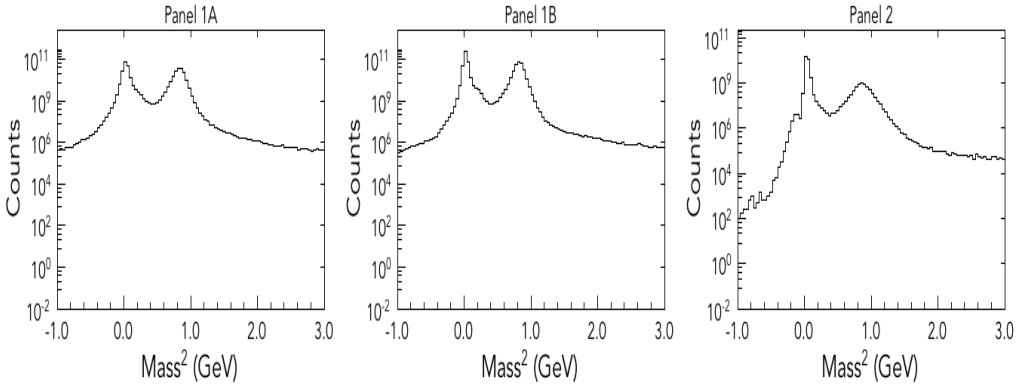

Fig. 29. Reconstructed mass squared (GeV^2) for positively charged particles for all counters in panel-1a (left), panel-1b (middle), and panel-2 (right) from beam data with a 10.6 GeV electron incident on a liquid-hydrogen target.

A plot of velocity versus momentum is shown in Fig. 30 for positively charged particles, displaying the overall particle identification possible with this detector through the separation of the different particle species. Here the distributions are presented separately for the counters in panel-1a, panel-1b, and panel-2 summed over all CLAS12 Forward Detector sectors. These distributions qualitatively show the particle separation for π/K, π/p, and K/p vs. momentum as required by the system specifications in Section 3 and Table 1.

6 Summary

We have designed and assembled a time-of-flight system for the Forward Detector of the new CLAS12 Spectrometer in Hall B at Jefferson Lab known as the Forward Time-of-Flight or FTOF detector. This system consists of 88

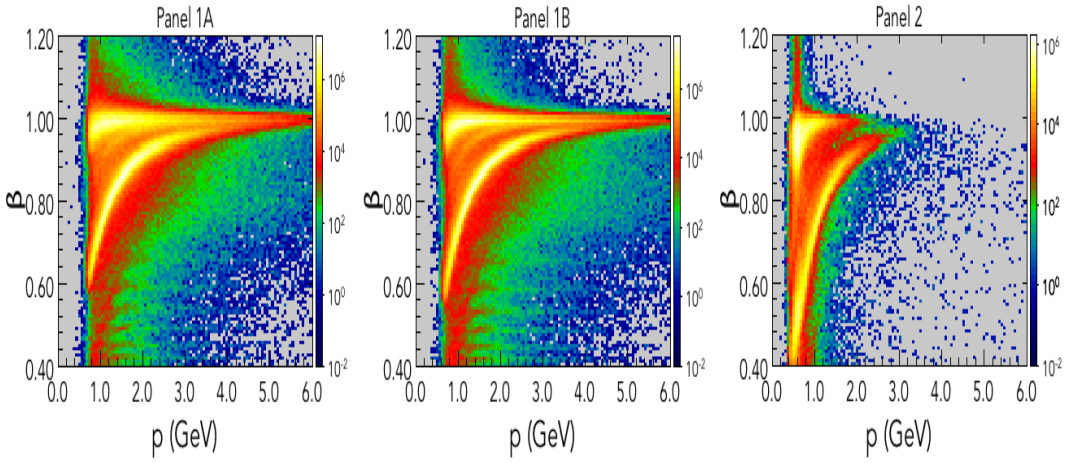

Fig. 30. (Color Online) Velocity of positive hadrons (β) versus momentum (GeV) for all counters in panel-1a (left), panel-1 (middle), and panel-2 (right) from beam data with a 10.6 GeV electron incident on a liquid-hydrogen target.

scintillation bars in each of the six forward sectors of the CLAS12 Forward Detector for a total of 540 counters. This design is based on rectangular counters varying in length from 17 cm long to 426 cm long in three different counter arrays in each sector. In the polar angle range from 5° to 35° the FTOF system consists of two layers of counters referred to as the panel-1a counters and the panel-1b counters. The panel-1a counters were refurbished from the forward TOF counters that were part of the original CLAS spectrometer. The panel-1b counters were newly constructed for CLAS12. Together the timing measurements from these counters provide time resolutions over all bars from 60 ps for the short counters at small angles to 100 ps for the long counters at large angles. In the polar angle range from 35° to 45° the FTOF system consists of the panel-2 counters that provide timing resolutions of ∼200 ps. With these timing resolutions the FTOF system can separate π/K to 2.8 GeV, K/p to 4.8 GeV, and π/p to 5.4 GeV with 4σ separation with up to an order of magnitude difference in the relative yields. The specifications are sufficient to meet to meet the particle identification requirements in the forward direction for the full CLAS12 physics program. The performance of the FTOF system was verified in extensive bench studies in our cosmic ray test stands as well as after installation in the first beam runs with the CLAS12 system in the period from Dec. 2017 to May 2018.

Acknowledgements

We benefited greatly from useful discussions with and assistance from Sergey Boyarinov, Chris Cuevas, Haiyan Lu, Cole Smith, Elton Smith, and Veronique Ziegler. We also thank the Hall B technical crew for their efforts during counter installation and cabling. This work was supported in part by DOE Contract #DE-AC05-84ER40150.

References

[1] B.A. Mecking *et al.*, Nucl. Inst. and Meth. **A503**, 513 (2003).

[2] V.D. Burkert *et al.*, to be published in Nucl. Inst. and Meth. A, (2020).

[3] E.S. Smith *et al.*, Nucl. Inst. and Meth. **A432**, 265 (1999).

[4] Bicron, 12345 Kinsman Road, Newbury, OH 44065, http://www.bicron.com.

[5] Hamamatsu Photonics, http://www.hamamatsu.com.

[6] R. Gothe, *A New Time-of-Flight System for CLAS12"*, to be submitted to Nucl. Inst. and Meth A, (2020).

[7] D.S. Carman, *Forward Time-of-Flight Geometry for CLAS12*, CLAS12-Note 2014-005. https://misportal.jlab.org/mis/physics/clas12/viewFile.cfm/2014-005.pdf?documentId=13

[8] M. Kuhlen, M. Moszynski, R. Stroynowski, E. Wicklund, and B. Milliken, Nucl. Instr. and Meth. **A301**, 223 (1991).

[9] https://www.crystals.saint-gobain.com/sites/imdf.crystals.com/files/documents/bc400-404-408-412-416-data-sheet.pdf

[10] ADIT Electron Tubes, 300 Crane St, Sweetwater, TX 79556

[11] Photonis Imaging Sensors, http://www.photonis.com

[12] D.S. Carman and V. Baturin, *CLAS12 FTOF Studies: Rate and Magnetic Shielding Effects on PMT Timing Resolutions*, CLAS-Note 2011-018. https://misportal.jlab.org/ul/Physics/Hall-B/clas/viewFile.cfm/2011-018.pdf?documentId=653

[13] http://www.caen.it/servlet/checkCaenManualFile?Id=12125

[14] E. Jastremski, https://www.jlab.org/Hall-B/ftof/manuals/caen-inl-notes.pdf

[15] https://www.jlab.org/Hall-B/ftof/manuals/FADC250UsersManual.pdf

[16] EPICS (Experimental Physics and Industrial Control System), http://www.aps.anl.gov/epics

[17] D.S. Carman, *CLAS12 FTOF Panel-1a and Panel-2 Refurbishment and Baseline Test Results*, CLAS12-Note 2013-001. https://misportal.jlab.org/mis/physics/clas12/viewFile.cfm/2013-001.pdf?documentId=1

[18] R.T. Giles, F.M. Pipkin, and J.P. Wolinski, Nucl. Instr. and Meth. A **252**, 41 (1986).

[19] T. Yamaoka, F. Kajino, I. Tada, S. Hayashi, *Absolute Number Calibration of Photoelectrons of Photomultiplier Tubes Using the Nature of Statistical Distribution*, Proceedings of the 28th International Cosmic Ray Conference, July 31 - August 7, 2003, editors: T. Kajita, Y. Asaoka, A. Kawachi, Y. Matsubara, and M. Sasaki, p. 2871 (2003).

[20] D.S. Carman, *Forward Time-of-Flight PMT Currents*, FTOF internal note, (2014). https://www.jlab.org/Hall-B/ftof/notes/ftof_currents.pdf

[21] D.S. Carman, *Description of the Calibration Algorithms for the CLAS12 Forward Time-of-Flight System*, https://www.jlab.org/Hall-B/ftof/notes/ftof_calib.pdf

[22] D.S. Carman, *Forward Time-of-Flight Reconstruction for CLAS12*, https://www.jlab.org/Hall-B/ftof/notes/ftof-recon.pdf

[23] CLAS12 GEANT4 Monte Carlo suite *gemc*, http://gemc.jlab.org.

[24] R. De Vita, D.S. Carman, C. Smith, S. Stepanyan, and M. Ungaro, *Study of the Electromagnetic Background Rates in CLAS12*, CLAS12-Note 2017-016. https://misportal.jlab.org/mis/physics/clas12/viewFile.cfm/2017-016.pdf?documentId=52